UNLEASHING THE POTENTIAL OF FRACTIONAL CALCULUS IN GRAPH NEURAL NETWORKS WITH FROND

Qiyu Kang[1]*, **Kai Zhao**[1]*, **Qinxu Ding**[2], **Feng Ji**[1], **Xuhao Li**[3], **Wenfei Liang**[1], **Yang Song**[4], **Wee Peng Tay**[1]
[1]Nanyang Technological University [2]Singapore University of Social Sciences
[3]Anhui University [4]C3 AI, Singapore

ABSTRACT

We introduce the FRactional-Order graph Neural Dynamical network (FROND), a novel learning framework that extends traditional continuous graph neural networks (GNNs), which are typically modeled as integer-order ordinary differential equations (ODEs). By incorporating the Caputo fractional derivative, FROND leverages the non-local properties of fractional calculus to capture long-term dependencies in feature updates. This approach contrasts sharply with the Markovian update mechanism inherent in conventional integer-order models and promises enhancements in graph representation learning. We offer an interpretation of the feature updating process on graphs from a non-Markovian random walk perspective when the feature updating is governed by a diffusion process. We demonstrate analytically that oversmoothing can be mitigated in this setting. Experimentally, we validate the FROND framework by comparing the fractional adaptations of various established integer-order continuous GNNs, demonstrating their consistently superior performance and underscoring the framework's potential as an effective extension to enhance traditional continuous GNNs. The code is available at `https://github.com/zknus/ICLR2024-FROND`.

1 INTRODUCTION

Graph Neural Networks (GNNs) have excelled in diverse domains, e.g., chemistry (Yue et al., 2019), finance (Ashoor et al., 2020), and social media (Kipf & Welling, 2017; Zhang et al., 2022; Wu et al., 2021). The message passing scheme (Feng et al., 2022), where features are aggregated along edges and iteratively propagated through layers, is crucial for the success of GNNs. Over the past few years, numerous types of GNNs have been proposed, including Graph Convolutional Networks (GCN) (Kipf & Welling, 2017), Graph Attention Networks (GAT) (Veličković et al., 2018), and GraphSAGE (Hamilton et al., 2017). Recent works, such as (Chamberlain et al., 2021c; Thorpe et al., 2022; Rusch et al., 2022; Song et al., 2022; Choi et al., 2023; Zhao et al., 2023; Kang et al., 2023), have incorporated various continuous dynamical processes to propagate information over the graph nodes, inspiring one class of continuous GNNs based on integer-order differential equations on graphs. These models have demonstrated notable performance, for instance, in enhancing robustness and addressing heterophilic graphs.

Within these integer-order continuous GNNs, the differential operator $\mathrm{d}^\beta / \mathrm{d}t^\beta$ has been constrained to *integer values* of β, primarily 1 or 2. However, over recent decades, the wider scientific community has explored fractional-order differential operators, where β can be any *real number*. These expansions have proven pivotal in various applications characterized by non-local and memory-dependent behaviors, with examples including viscoelastic materials (Bagley & Torvik, 1983), anomalous transport mechanisms (Gómez-Aguilar et al., 2016), and fractal media (Mandelbrot & Mandelbrot, 1982). Unlike conventional integer-order derivatives that measure the function's *instantaneous rate of change* and focus on the local vicinity, fractional-order derivatives (Tarasov, 2011) consider *the entire historical trajectory of the function*. For detailed definitions of fractional-order derivatives, readers are referred to Section 2.1 and Appendix B.

*First two authors contributed equally. Correspondence to: Qiyu Kang <kang0080@e.ntu.edu.sg>.

We introduce the FRactional-Order graph Neural Dynamical network (FROND) framework, a new approach that broadens the capabilities of traditional integer-order continuous GNNs by incorporating fractional calculus. It naturally generalizes the integer-order derivative $\mathrm{d}^\beta / \mathrm{d}t^\beta$ in these GNNs to accommodate any positive real number β. This modification gives FROND the ability to incorporate *memory-dependent dynamics* for information propagation and feature updating, enabling refined graph representations and improved performance potentially. Importantly, this technique assures at least equivalent performance to integer-order models, as setting β to integer values reverts the models to their traditional integer-order forms.

Several works like (Maskey et al., 2023) have incorporated fractional graph shift operators within graph neural ODE models. These studies are distinct from our research, wherein we focus on incorporating time-fractional derivatives for updating graph node features, modeled as a memory-inclusive dynamical process. Other works like (Liu et al., 2022) have used fractional calculus in gradient propagation for the training process, which is different from leveraging fractional differential equations (FDEs) in modeling the node feature updating. We provide a detailed discussion of the differences between FROND and these other works in Appendix A.

Many real-world graph datasets, such as the World Wide Web, the Internet, and various biological and social networks, are known to exhibit scale-free hierarchical structures. These structures suggest a pervasive self-similarity across different scales, hinting at an underlying fractal behavior (Song et al., 2005; Kim et al., 2007; Masters, 2004). It has been well-established that dynamical processes with self-similarity on such fractal media are more accurately described using fractional differential equations (FDEs). For instance, the dispersion of heat or mass over these structures is best modeled using fractional diffusion equations (Diaz-Diaz & Estrada, 2022). Further investigations have revealed a direct connection between the fractal dimension of these structures and the order β in fractional derivatives $\mathrm{d}^\beta / \mathrm{d}t^\beta$ (Nigmatullin, 1992; Tarasov, 2011). This revelation births a compelling insight: the optimal β in our models, which may differ from integers, can pave the way for enhanced node classification and potentially unearth insights into the inherent "fractal" nature of graph datasets.

Main contributions. Our objective in this paper is to formulate a generalized fractional-order continuous GNN framework. Our key contributions are summarized as follows:

- We propose a novel, generalized continuous GNN framework that incorporates non-local fractional derivatives $\mathrm{d}^\beta / \mathrm{d}t^\beta$. This framework generalizes the prior class of integer-order continuous GNNs (Chamberlain et al., 2021c; Thorpe et al., 2022; Rusch et al., 2022; Song et al., 2022; Choi et al., 2023; Zhao et al., 2023), subsuming them as special instances with β setting as integers. This approach also lays the groundwork for a diverse new class of GNNs that can accommodate a broad array of learnable memory-dependent feature-updating processes.
- We provide an interpretation from the perspective of a non-Markovian graph random walk when the feature-updating dynamics are inspired by the fractional heat diffusion process. Contrasting with the Markovian random walk implicit in traditional integer-order graph neural diffusion models whose convergence to the stationary equilibrium is exponentially swift, we establish that in FROND, convergence follows an algebraic rate. This characteristic enhances FROND's ability to mitigate oversmoothing, as verified by our experimental results.
- We underscore the compatibility of FROND, emphasizing its capability to be seamlessly integrated to augment the performance of existing integer-order continuous GNNs across diverse datasets. Our exhaustive experiments, encompassing the fractional differential extension of (Chamberlain et al., 2021c; Thorpe et al., 2022; Rusch et al., 2022; Song et al., 2022; Choi et al., 2023; Zhao et al., 2023), substantiate this claim. Through detailed ablation studies, we provide insights into the choice of numerical schemes and parameters.

2 Preliminaries

In this section, we briefly introduce fractional calculus and integer-order continuous GNNs. For a comprehensive review of fractional calculus, readers are referred to Appendix B.

2.1 Caputo Fractional Derivative

The literature offers various fractional derivative definitions, notably by Riemann, Liouville, Chapman, and Caputo (Tarasov, 2011). Our study leverages the *Caputo* fractional derivative, due to the reasons

listed in Appendix B.4. The traditional first-order derivative of a scalar function $f(t)$ represents the local rate of change of the function at a point, defined as: $\frac{\mathrm{d}f(t)}{\mathrm{d}t} = \lim_{\Delta t \to 0} \frac{f(t+\Delta t)-f(t)}{\Delta t}$. Let $F(s)$ denote the Laplace transform of $f(t)$, assumed to exist on $[s_0, \infty)$ for some $s_0 \in \mathbb{R}$. Under certain conditions (Korn & Korn, 2000), the Laplace transform of $\frac{\mathrm{d}f(t)}{\mathrm{d}t}$ is given by:

$$\mathcal{L}\left\{\frac{\mathrm{d}f(t)}{\mathrm{d}t}\right\} = sF(s) - f(0) \tag{1}$$

The Caputo fractional derivative of order $\beta \in (0, 1]$ for a function $f(t)$ is defined as follows:

$$D_t^\beta f(t) = \frac{1}{\Gamma(1-\beta)} \int_0^t (t-\tau)^{-\beta} f'(\tau)\, \mathrm{d}\tau, \tag{2}$$

where $\Gamma(\cdot)$ denotes the gamma function, and $f'(\tau)$ is the first-order derivative of f. The broader definition for any $\beta > 0$ is deferred to Appendix B. The Caputo fractional derivative inherently integrates the entire history of the system through the integral term, emphasizing its non-local nature. For $s > \max\{0, s_0\}$, the Laplace transform of the Caputo fractional derivative is given by (Diethelm, 2010)[Theorem 7.1]:

$$\mathcal{L}\left\{D_t^\beta f(t)\right\} = s^\beta F(s) - s^{\beta-1} f(0). \tag{3}$$

Comparing (1) and (3), it is evident that the Caputo derivative serves as a generalization of the first-order derivative. The alteration in the exponent of s comes from the memory-dependent property in (2), enabling the development of enhanced continuous GNN models. As $\beta \to 1$, the Laplace transform of the Caputo fractional derivative converges to that of the traditional first-order derivative. This is because when $\beta = 1$, $D_t^1 f = f'$ is uniquely determined through the inverse Laplace transform (Cohen, 2007).

In summary, from the frequency domain using the Laplace transform, we observe that the Caputo fractional derivative can be seen as a natural extension of the traditional first-order derivative. For vector-valued functions, this derivative is defined component-wise for each dimension.

2.2 Integer-Order Continuous GNNs

We denote an undirected graph as $\mathcal{G} = (\mathcal{V}, \mathbf{W})$, where $\mathcal{V}$ is the set of $|\mathcal{V}| = N$ nodes. The feature matrix $\mathbf{X} = \left([\mathbf{x}_1]^\intercal, \cdots, [\mathbf{x}_N]^\intercal\right)^\intercal \in \mathbb{R}^{N \times d}$ consists of rows $\mathbf{x}_i \in \mathbb{R}^d$ as node feature vectors and i is the node index. The $N \times N$ matrix $\mathbf{W} := (W_{ij})$ has elements W_{ij} indicating the edge weight between the i-th and j-th node with $W_{ij} = W_{ji}$. The subsequent feature updating process leverages ODEs to facilitate information propagation amongst graph nodes with initial condition $\mathbf{X}(0) = \mathbf{X}$. We present prevalent integer-order continuous GNNs from the literature as follows.

GRAND: Inspired by the heat diffusion equation, GRAND (Chamberlain et al., 2021c) utilizes the following nonlinear autonomous dynamical system:

$$\frac{\mathrm{d}\mathbf{X}(t)}{\mathrm{d}t} = (\mathbf{A}(\mathbf{X}(t)) - \mathbf{I})\mathbf{X}(t). \tag{4}$$

where $\mathbf{A}(\mathbf{X}(t))$ is a learnable, time-variant attention matrix, calculated using the features $\mathbf{X}(t)$, and $\mathbf{I}$ denotes the identity matrix. The feature update outlined in (4) is referred to as the **GRAND-nl** version (due to the nonlinearity in $\mathbf{A}(\mathbf{X}(t))$). We define $d_i = \sum_{j=1}^n W_{ij}$ and let $\mathbf{D}$ be a diagonal matrix with $D_{ii} = d_i$. The *random walk Laplacian* is then represented as $\mathbf{L} = \mathbf{I} - \mathbf{W}\mathbf{D}^{-1}$. In a simplified context, we employ the following linear dynamical system:

$$\frac{\mathrm{d}\mathbf{X}(t)}{\mathrm{d}t} = (\mathbf{W}\mathbf{D}^{-1} - \mathbf{I})\mathbf{X}(t) = -\mathbf{L}\mathbf{X}(t). \tag{5}$$

The feature update process in (5) is the **GRAND-l** version. For implementations of (5), one may direct set $\mathbf{W}\mathbf{D}^{-1} = \mathbf{A}(\mathbf{X}(0))$ as a column-stochastic attention matrix, rather than using a plain weight. Notably, in this time-invariant setting, the attention weight matrix, reliant on the initial node features, stays unchanged throughout the feature evolution period.

GRAND++ (Thorpe et al., 2022) adds a source term to graph neural diffusion, enhancing learning in scenarios with limited labeled nodes. **GraphCON** (Rusch et al., 2022) employs a second-order ODE,

which is equivalent to two first-order ODEs, drawing inspiration from oscillator systems. **CDE** (Zhao et al., 2023) incorporates convection-diffusion equations into GNNs to address heterophilic graph challenges. **GREAD** (Choi et al., 2023) introduces a reaction term in the GRAND model, improving its application to heterophilic graphs and formulating a diffusion-reaction equation within GNNs. The detailed formulation for each model is presented in Appendix E.1.

3 FRACTIONAL-ORDER GRAPH NEURAL DYNAMICAL NETWORK

In this section, we introduce the FROND framework, a novel approach that augments traditional integer-order continuous GNNs by incorporating fractional calculus. We elucidate the fractional counterparts of several well-established integer-order continuous GNNs, including GRAND, GRAND++, GraphCON, CDE, and GREAD, as referenced in Section 2.2. We provide a detailed study of the fractional extension of GRAND, and present insights into the inherent memory mechanisms of fractional calculus through a random walk interpretation. Our theoretical findings suggest a potential mitigation of over-smoothness due to the model's algebraic convergence to stationarity. Subsequently, we outline the numerical FDE solvers required to implement FROND.

3.1 FRAMEWORK

Consider a graph $\mathcal{G} = (\mathcal{V}, \mathbf{W})$ as defined in Section 2.2. Analogous to the implementation in traditional integer-order continuous GNNs, a preliminary learnable encoder function $\varphi : \mathcal{V} \to \mathbb{R}^d$ that maps each node to a feature vector can be applied. Stacking all the feature vectors together, we obtain $\mathbf{X} \in \mathbb{R}^{N\times d}$. Employing the Caputo fractional derivative outlined in Section 2.1, the information propagation and feature updating dynamics in FROND are characterized by the following FDE:

$$D_t^\beta \mathbf{X}(t) = \mathcal{F}(\mathbf{W}, \mathbf{X}(t)), \quad \beta > 0, \tag{6}$$

where β denotes the fractional order of the derivative, and $\mathcal{F}$ is a dynamic operator on the graph like the models presented in Section 2.2. The initial condition for (6) is set as $\mathbf{X}^{[\lceil\beta\rceil-1]}(0) = \ldots = \mathbf{X}(0) = \mathbf{X}$ consisting of the preliminary node features, with $\mathbf{X}^{[i]}(t)$ denoting the i-th order derivative and $\lceil\beta\rceil$ is the smallest integer not less than β, akin to the initial conditions seen in integer-order ODEs.[1] Similar to integer-order continuous GNNs, we set an integration time parameter T to compute $\mathbf{X}(T)$. The final node embeddings for downstream tasks are then decoded using a learnable decoder $\psi(\mathbf{X}(T))$.

When $\beta = 1$, (6) reverts to the class of integer-order continuous GNNs, with the infinitesimal variation of features dependent only on their present state. Conversely, when $\beta < 1$, the Caputo fractional derivative definition (2) dictates that the updating process for features encompasses their entire history, not just the present state. This paradigm facilitates memory-dependent dynamics in the model. For further insights into memory dependence, readers are directed to Section 3.3, which discusses time discretization techniques for numerically solving the system. This section illustrates how, akin to integer-order ODE models, time acts consistently as an analog to the layer index and how the non-local properties of fractional derivatives facilitate nontrivial dense or skip connections between layers. In Section 3.2, when the dynamic operator $\mathcal{F}$ is designated as the diffusion process in (5), we offer a memory-dependent *non-Markov* random walk interpretation of the fractional graph neural diffusion process. Here, as $\beta \to 1$, the non-Markov random walk increasingly detaches from the path history, becoming a Markov walk at $\beta = 1$, which is related to the normal diffusion process (Thorpe et al., 2022). The parameter β provides flexibility to adjust the extent of memorized dynamics embedded in the framework. Additionally, as discussed in Section 1, the information propagation dynamics in fractal graph datasets may be better represented using FDEs. Choosing a non-integer β could reveal the degree of fractality in graph datasets.

3.1.1 FROND MODEL EXAMPLES

When $\mathcal{F}$ in (6) is specified to the dynamics depicted in various integer-order continuous GNNs (cf. Section 2.2), we formulate FROND GNN variants such as F-GRAND, F-GRAND++, F-GREAD, F-CDE, and F-GraphCON, serving as fractional differential extensions of the original GNNs.

[1] In the main paper, we mainly consider $\beta \in (0, 1]$ and the initial condition is $\mathbf{X}(0) = \mathbf{X}$. See Appendix B.3.2.

F-GRAND: Mirroring the GRAND model, the fractional GRAND (F-GRAND) is divided into two versions. The F-GRAND-nl employs a time-variant FDE as follows:

$$D_t^\beta \mathbf{X}(t) = (\mathbf{A}(\mathbf{X}(t)) - \mathbf{I})\mathbf{X}(t), \quad 0 < \beta \leq 1. \tag{7}$$

It is computed using $\mathbf{X}(t)$ and the attention mechanism derived from the Transformer model (Vaswani et al., 2017). The entries of $\mathbf{A}(\mathbf{X}(t))$ are given by:

$$a(\mathbf{x}_i, \mathbf{x}_j) = \mathrm{softmax}\left(\frac{(\mathbf{W}_K \mathbf{x}_i)^\top \mathbf{W}_Q \mathbf{x}_j}{d_k}\right). \tag{8}$$

In this formulation, $\mathbf{W}_K$ and $\mathbf{W}_Q$ are the learned matrices, and d_k signifies a hyperparameter defining the dimensionality of W_K. In parallel, the F-GRAND-l version stands as the fractional differential extension of (5):

$$D_t^\beta \mathbf{X}(t) = -\mathbf{L}\mathbf{X}(t), \quad 0 < \beta \leq 1. \tag{9}$$

F-GRAND++, F-GREAD, F-CDE, and F-GraphCON: Due to space constraints, we direct the reader to Appendix E for detailed formulations. Succinctly, they represent the fractional differential extensions of GRAND++, GraphCON, CDE, and GREAD. To highlight FROND's compatibility and its potential to enhance the performance of existing integer-order continuous GNNs across a variety of datasets, exhaustive experiments are provided in Section 4 and Appendix E.

3.2 Random Walk Perspective of F-GRAND-l

The established Markov interpretation of GRAND-l (5), as outlined in (Thorpe et al., 2022), aligns with F-GRAND-l (9) when $\beta = 1$. We herein broaden this interpretation to encompass non-Markov random walks when β is a non-integer, thereby elucidating the memory effects inherent in FROND through a consideration of the walker's path history. In contrast to the Markovian walk, which converges exponentially to equilibrium, our strategy assures algebraic convergence, enhancing F-GRAND-l's efficacy in mitigating oversmoothing as evidenced in Section 4.3.

To begin, we discretize the time domain into time instants as $t_n = n\sigma, \sigma > 0, n = 0, 1, 2, \ldots$, where σ is assumed to be small enough to ensure the validity of the approximation. Let $\mathbf{R}(t_n)$ be a random walk on the graph nodes $\{\mathbf{x}_j\}_{j=1}^N$ that is not necessarily a Markov process and $\mathbf{R}(t_{n+1})$ may depend on the path history $(\mathbf{R}(t_0), \mathbf{R}(t_1), \ldots, \mathbf{R}(t_n))$ of the random walker. For convenience, we introduce the coefficients c_k for $k \geq 1$ and b_m for $m \geq 0$ from (Gorenflo et al., 2002), which are used later to define the random walk transition probability:

$$c_k(\beta) = (-1)^{k+1}\binom{\beta}{k} = \left|\binom{\beta}{k}\right|, \quad b_m(\beta) = \sum_{k=0}^{m}(-1)^k\binom{\beta}{k}, \tag{10}$$

where the generalized binomial coefficient $\binom{\beta}{k} = \frac{\Gamma(\beta+1)}{\Gamma(k+1)\Gamma(\beta-k+1)}$ and the gamma function Γ are employed in the definition of the coefficients. The sequences c_k and b_m consist of positive numbers, not greater than 1, decreasing strictly monotonically to zero (see supplementary material for details) and satisfy $\sum_{k=1}^n c_k + b_n = 1$. Using these coefficients, we define the transition probabilities of the random walk starting from $\mathbf{x}_{j_0}$ as

$$\begin{aligned}
&\mathbb{P}\big(\mathbf{R}(t_{n+1}) = \mathbf{x}_{j_{n+1}} \,\big|\, \mathbf{R}(t_0) = \mathbf{x}_{j_0}, \mathbf{R}(t_1) = \mathbf{x}_{j_1}, \ldots, \mathbf{R}(t_n) = \mathbf{x}_{j_n}\big) \\
&= \begin{cases}
c_1 - \sigma^\beta & \text{if staying at current location with } j_{n+1} = j_n, \\
\sigma^\beta \frac{W_{j_n j_{n+1}}}{d_{j_n}} & \text{if jumping to neighboring nodes with } j_{n+1} \neq j_n, \\
c_{n+1-k} & \text{if revisiting historical positions with } j_{n+1} = j_k, 1 \leq k \leq n-1, \\
b_n & \text{if revisiting historical positions with } j_{n+1} = j_0.
\end{cases}
\end{aligned} \tag{11}$$

This formulation integrates memory effects, considering the walker's time, position, and path history. The transition mechanism of the memory-inclusive random walk between t_n and t_{n+1} is elucidated as follows: Suppose the walker is at node j_n at time t_n, having a full path history $(j_0, j_1, \ldots, j_n)$. Generating a uniform random number $0 \leq \rho < 1$, we divide the interval $[0, 1)$ into adjacent sub-intervals with lengths $c_1, c_2, \ldots, c_n, b_n$. We further subdivide the first interval (with length c_1) into sub-intervals of lengths $c_1 - \sigma^\beta$ and σ^β.

1. If ρ is in the first interval with length c_1, the walker either moves to a neighbor $j_{n+1} = k$ with probability $\sigma^\beta \frac{W_{j_n k}}{d_{j_n}}$ or remains at the current position with probability $c_1 - \sigma^\beta$.

2. For ρ in subsequent intervals, the walker jumps to a previously visited node in the history $(j_0, j_1, \ldots, j_{n-1})$, specifically, to j_{n+1-k} if in c_k, or to j_0 if in b_n.

When $\beta < 1$, the random walk can, with positive probability, revisit its history, which prevents the walker from drifting too far away from its local region. Using the technique from (Gorenflo et al., 2002), we can prove the following:

Theorem 1. *When $\sigma \to 0$ and $n\sigma = t$, $\mathbb{E}_i \mathbf{R}(t_n)$ converges to $\mathbf{x}_i(t)$, the i-th component of the solution $\mathbf{X}(t)$ to* (9)*. Here, $\mathbb{E}_i$ denotes the expectation over the random walk, defined by transition probabilities in* (11)*, which begins at node i with initial distribution $\mathbf{R}(0) = \mathbf{x}_i$, with probability 1.*

Remark 1. *Theorem 1 relates F-GAND-l* (9) *to the non-Markovian random walk in* (11)*, illustrating memory dependence in FROND. As $\beta \to 1$, this process reverts to the Markov random walk found in GRAND-l (Thorpe et al., 2022) in* (12)*. It underscores the FROND framework's capability to apprehend more complex dynamics than integer-order continuous GNNs.*

$$\mathbb{P}\big(\mathbf{R}(t_{n+1}) = \mathbf{x}_{j_{n+1}} \,\big|\, \mathbf{R}(t_0) = \mathbf{x}_{j_0}, \mathbf{R}(t_1) = \mathbf{x}_{j_1}, \ldots, \mathbf{R}(t_n) = \mathbf{x}_{j_n}\big) \tag{12}$$

$$= \mathbb{P}\big(\mathbf{R}(t_{n+1}) = \mathbf{x}_{j_{n+1}} \,\big|\, \mathbf{R}(t_n) = \mathbf{x}_{j_n}\big) = \begin{cases} 1-\sigma & \text{if staying at current location with } j_{n+1} = j_n \\ \sigma \frac{W_{j_n j_{n+1}}}{d_{j_n}} & \text{if jumping to neighbors with } j_{n+1} \neq j_n \end{cases}$$

since we have that all these coefficients vanishing except $c_1 = 1$, i.e.,

$$c_1 = 1, \quad \lim_{\beta \to 1} c_k(\beta) = 0, \quad k \geq 2, \quad \lim_{\beta \to 1} b_m = 0, \quad m \geq 1. \tag{13}$$

The approximation solution to (9) *at $\beta = 1$ via the Markov random walk* (12) *is established in (Thorpe et al., 2022). Similarly, in the continuous domain, a solution to the heat equation can be represented by random Brownian motion from the positions (Durrett, 2019).*

3.2.1 Oversmoothing Mitigation of F-GRAND-l Compared to GRAND-l

The stationary distribution for the Markov random walk, as given by (12), is recognized as $\boldsymbol{\pi} = (\frac{d_1}{\sum_{j=1}^N d_j}, \ldots, \frac{d_N}{\sum_{j=1}^N d_j})$. *The seminal research (Oono & Suzuki, 2020)[Corollary 3. and Remark 1] has incisively underscored that GNN oversmoothing is the exponential convergence to the stationary distribution when considering a GNN as a layered dynamical system.* More specifically, according to (Chung, 1997), we have the fast *exponential convergence* for GRAND-l as $\|\mathbb{P}(\mathbf{R}(t_n)) - \boldsymbol{\pi}^\intercal\|_2 \sim O(e^{-r'n})$[2], where $\mathbb{P}(\mathbf{R}(t_n))$ is the probability column vector, with its j-th element given as $\mathbb{P}(\mathbf{R}(t_n) = \mathbf{x}_j)$. Here, r' is a positive value related to the eigenvalues of the matrix $\mathbf{L}$, and $\|\cdot\|_2$ denotes the ℓ^2 norm. The continuous limit also shows analogous exponential convergence with $r > 0$:

$$\|\mathbb{P}(\mathbf{R}(t)) - \boldsymbol{\pi}^\intercal\|_2 \sim O(e^{-rt}). \tag{14}$$

In contrast, we next prove that the non-Markovian random walk with memory, as defined in (11), converges to the stationary distribution at a *slow algebraic rate*, thereby helping to mitigate oversmoothing. As $\beta \to 0$, the convergence is expected to be *arbitrarily slow*. In real-world scenarios where we operate within a finite horizon, this slower rate of convergence may be sufficient to alleviate oversmoothing, particularly when it is imperative for a deep model to extract distinctive features instead of achieving exponentially fast convergence to a stationary distribution.

Theorem 2. *Under the assumption that the graph is strongly connected and aperiodic, the stationary probability for the non-Markov random walk* (11)*, with $0 < \beta < 1$, is $\boldsymbol{\pi} = (\frac{d_1}{\sum_{j=1}^N d_j}, \ldots, \frac{d_N}{\sum_{j=1}^N d_j})$, which is unique. This mirrors the stationary probability of the Markovian random walk as defined by* (12) *when $\beta = 1$. Notably, when $\beta < 1$, the convergence of the distribution (distinct from $\boldsymbol{\pi}$) to $\boldsymbol{\pi}$ is algebraic:*

$$\|\mathbb{P}(\mathbf{R}(t)) - \boldsymbol{\pi}^\intercal\|_2 \sim \Theta(t^{-\beta}). \tag{15}$$

Remark 2. *For clarity, Theorem 2 indicates that the feature $\mathbf{x}_i(t)$, for all node i, is converging to the same stationary feature equilibrium $\mathbf{x_s} := \sum_k \frac{\mathbf{x}_k d_k}{\sum_{j=1}^N d_j}$ at a slow algebraic rate. More specifically:*

$$\|\mathbf{x}_i(t) - \mathbf{x_s}\|_2^2 = \|\sum_k \mathbf{x}_{(k)}[\mathbb{P}_i(\mathbf{R}(t))_k - \boldsymbol{\pi}_k]\|_2^2 = \Theta\left(t^{-2\beta}\right) \text{ for all node } i. \tag{16}$$

where $\mathbb{P}_i$ refers to that we have the initial probability as a one-hot vector with the i-th component being 1. This is because Theorem 2 confirms $\|\boldsymbol{\pi}_k - \mathbb{P}_i(\mathbf{R}(t))_k\| = \Theta\left(t^{-\beta}\right)$ for some k.

[2]We use the asymptotic order notations from (Notations, 2023) in this paper.

In (Rusch et al., 2022), the phenomenon of over-smoothness is defined through the exponential convergence of Dirichlet energy to zero. However, the following Corollary 1 establishes that the Dirichlet energy of F-GRAND-l converges algebraically to zero, mitigating over-smoothness issues as corroborated by the plots in Section 4.3 and Appendix D.7.

Corollary 1. *The Dirichlet energy,* $\mathbf{E}(\mathbf{X}(t))$*, with* $\mathbf{X}(t)$ *being the solution to* (9)*, has the convergence rate* $\Theta(t^{-2\beta})$*. Here, Dirichlet energy* $\mathbf{E}(\mathbf{X}(t))$ *is formally defined as*

$$\mathbf{E}(\mathbf{X}(t)) := \sum_{i\in\mathcal{V}}\sum_{j\in\mathcal{V}} \|\mathbf{x}_i(t) - \mathbf{x}_j(t)\|_2^2 \tag{17}$$

3.3 Solving FROND

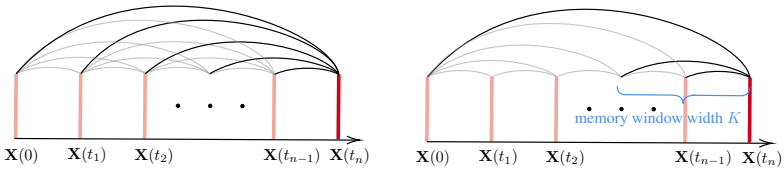

Figure 1: Diagrams of fractional Adams–Bashforth–Moulton method with full (left) and short (right) memory.

The studies by (Chen et al., 2018b; Quaglino et al., 2019; Yan et al., 2018) introduce numerical solvers specifically designed for integer-order neural ODE models. Our research, in contrast, engages with fractional-order ODEs, entities inherently more intricate than integer-order ODEs. To address the scenario *where* β *is non-integer*, we introduce the *fractional explicit Adams–Bashforth–Moulton method*, incorporating three variants employed in this study: the **basic predictor** discussed in this section, the **predictor-corrector** elaborated in Appendix C.2, and the **short memory principle** detailed in Appendix C.3. Additionally, we present one **implicit L1** solver in Appendix C.4. These methods exemplify how time still acts as a continuous analog to the layer index and elucidate how memory dependence manifests as nontrivial dense or skip connections between layers (see Figs. 1 and 4), stemming from the non-local properties of fractional derivatives.

Basic Predictor: We first employ a preliminary numerical solver called "predictor" (Diethelm et al., 2004) through time discretisation. Let h be a small positive discretization parameter:

$${}_{\mathrm{P}}\mathbf{X}^{(k)} = \sum_{j=0}^{\lceil\beta\rceil-1} \frac{t_k^j}{j!}\mathbf{X}^{[j]}(0) + \frac{1}{\Gamma(\beta)}\sum_{j=0}^{k-1}\mu_{j,k}\mathcal{F}(\mathbf{W},\mathbf{X}^{(j)}), \tag{18}$$

where $\mu_{j,n} = \frac{h^\beta}{\beta}\left((n-j)^\beta - (n-1-j)^\beta\right)$, k denotes the discrete time index (iteration), and $t_k = kh$ represents the discretized time steps. $\mathbf{X}^{(k)}$ is the numerical approximation of $\mathbf{X}(t_k)$. When $\beta = 1$, this method simplifies to the Euler solver in (Chen et al., 2018b; Chamberlain et al., 2021c) as $\mu_{j,n} \equiv h$, yielding ${}_{\mathrm{P}}\mathbf{X}^{(k)} = \mathbf{X}^{(k-1)} + h\mathcal{F}(\mathbf{W},\mathbf{X}^{(k-1)})$. Thus, our basic predictor can be considered as the fractional Euler method or fractional Adams–Bashforth method, which is a generalization of the Euler method used in (Chen et al., 2018b; Chamberlain et al., 2021c). However, when $\beta < 1$, we need to utilize the full memory $\{\mathcal{F}(\mathbf{W},\mathbf{X}^{(j)})\}_{j=0}^{k-1}$. The block diagram in Fig. 1 shows the basic predictor and the short memory variant, highlighting the inclusion of nontrivial dense or skip connections in our framework. A more refined visualization is conveyed in Fig. 4, elucidating the manner in which information propagates through layers and the graph's spatial domain.

4 Experiments

We execute a series of experiments to illustrate that integer-order continuous GNNs, structured under the FROND framework and utilizing D_t^β, achieve superior performance compared to the traditional models reliant on the $\frac{\mathrm{d}}{\mathrm{d}t}$ approach. *Importantly, our primary aim is not to achieve state-of-the-art results, but rather to demonstrate the additional effectiveness of the FROND framework when applied to existing integer-order continuous GNNs.* In the main paper, we detail the impressive results achieved by F-GRAND, particularly emphasizing its efficacy on tree-structured data, and F-CDE, highlighting its proficiency in managing large heterophilic datasets. We also further validate the slow algebraic convergence, as discussed in Theorem 2, by constructing deeper GNNs with non-integer $\beta < 1$. To maintain consistency in the experiments presented in the main paper, the basic predictor solver is used instead of other solvers when $\beta < 1$.

More Experiments In the Appendix: The Appendix D section provides additional details covering various aspects such as experimental settings, described in Appendices D.1 to D.3, the performance of different solver variants in Appendix D.5, the computational complexity of F-GRAND in Appendix D.6, and analysis of F-GRAND's robustness against adversarial attacks in Appendix D.9. Furthermore, results related to other FROND-based integer-order continuous GNNs are extensively presented in the Appendix E. In the main text, we utilize the basic predictor, as delineated in (18), while the exploration of its variants is reserved for the Appendix D.5. The fractal dimensions of some datasets are computed using the Compact-Box-Burning algorithm (Song et al., 2007). The correlation between fractional dimension and the optimal fractional-derivative order β, steering the extent of memorized dynamics over graph datasets, is delineated in Appendix D.11.

Table 1: Node classification results(%) for random train-val-test splits. The best and the second-best results are highlighted in **red** and **blue**, respectively.

Method	Cora	Citeseer	Pubmed	CoauthorCS	Computer	Photo	CoauthorPhy	ogbn-arxiv	Airport	Disease
GCN	81.5±1.3	71.9±1.9	77.8±2.9	91.1±0.5	82.6±2.4	91.2±1.2	92.8±1.0	72.2±0.3	81.6±0.6	69.8±0.5
GAT	81.8±1.3	71.4±1.9	78.7±2.3	90.5±0.6	78.0±19.0	85.7±20.3	92.5±0.90	**73.7±0.1**	81.6±0.4	70.4±0.5
HGCN	78.7±1.0	65.8±2.0	76.4±0.8	90.6±0.3	80.6±1.8	88.2±1.4	90.8±1.5	59.6±0.4	85.4±0.7	89.9±1.1
GIL	82.1±1.1	71.1±1.2	77.8±0.6	89.4±1.5	–	89.6±1.3	–	–	91.5±1.7	**90.8±0.5**
GRAND-l	**83.6±1.0**	73.4±0.5	78.8±1.7	92.9±0.4	83.7±1.2	92.3±0.9	93.5±0.9	71.9±0.2	80.5±9.6	74.5±3.4
GRAND-nl	82.3±1.6	70.9±1.0	77.5±1.8	92.4±0.3	82.4±2.1	92.4±0.8	91.4±1.3	71.2±0.2	90.9±1.6	81.0±6.7
F-GRAND-l	**84.8±1.1**	**74.0±1.5**	**79.4±1.5**	**93.0±0.3**	**84.4±1.5**	**92.8±0.6**	**94.5±0.4**	**72.6±0.1**	**98.1±0.2**	**92.4±3.9**
β for F-GRAND-l	0.9	0.9	0.9	0.7	0.98	0.9	0.6	0.7	0.5	0.6
F-GRAND-nl	83.2±1.1	**74.7±1.9**	**79.2±0.7**	**92.9±0.4**	**84.1±0.9**	**93.1±0.9**	**93.9±0.5**	71.4±0.3	**96.1±0.7**	85.5±2.5
β for F-GRAND-nl	0.9	0.9	0.4	0.6	0.85	0.8	0.4	0.7	0.1	0.7

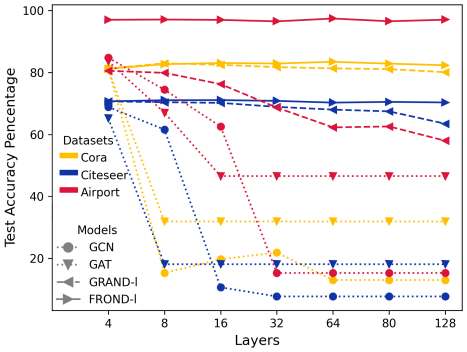

Figure 2: oversmoothing mitigation.

Table 2: Graph classification results.

Feature	POL Profile	POL word2vec	POL BERT	GOS Profile	GOS word2vec	GOS BERT
GraphSage	77.60±0.68	80.36±0.68	81.22±4.81	92.10±0.08	96.58±0.22	**97.07±0.23**
GCN	**78.28±0.52**	83.89±0.53	83.44±0.38	89.53±0.49	96.28±0.08	95.96±0.75
GAT	74.03±0.53	78.69±0.78	82.71±0.19	91.18±0.23	96.57±0.34	96.61±0.45
GRAND-l	77.83±0.37	**86.57±1.13**	**85.97±0.74**	**96.11±0.26**	**97.04±0.55**	96.77±0.34
F-GRAND-l	**79.49±0.43**	**88.69±0.37**	**89.29±0.93**	**96.40±0.19**	**97.40±0.03**	**97.53±0.14**

Table 3: Node classification accuracy of F-GRAND-l under different value of β when time $T = 8$.

β	0.1	0.3	0.5	0.7	0.9	1.0
Cora	74.80±0.42	77.0±0.98	79.60±0.91	81.56±0.30	82.68±0.64	82.37±0.59
Airport	97.09±0.87	95.80±2.03	91.66±6.34	84.36±8.04	78.73±6.33	78.88±9.67

4.1 Node Classification of F-GRAND

Datasets and splitting. We utilize datasets with varied topologies, including citation networks (Cora (McCallum et al., 2004), Citeseer (Sen et al., 2008), Pubmed (Namata et al., 2012)), tree-structured datasets (Disease and Airport (Chami et al., 2019)), coauthor and co-purchasing graphs (CoauthorCS (Shchur et al., 2018), Computer and Photo (McAuley et al., 2015)), and the ogbn-arxiv dataset (Hu et al., 2020). We follow the same data splitting and pre-processing in (Chami et al., 2019) for Disease and Airport datasets. Consistent with experiment settings in GRAND (Chamberlain et al., 2021c), we use random splits for the largest connected component of each other dataset. We also incorporate the large-scale Ogbn-Products dataset (Hu et al., 2021) to demonstrate the scalability of the FROND framework, with the results displayed in Table 7.

Methods. For a comprehensive performance comparison, we select several prominent GNN models as baselines, including GCN (Kipf & Welling, 2017), and GAT (Veličković et al., 2018). Given the inclusion of tree-structured datasets, we also incorporate well-suited baselines: HGCN(Chami et al., 2019) and GIL (Zhu et al., 2020b). To highlight the benefits of memorized dynamics in FROND, we include GRAND (Chamberlain et al., 2021c) as a special case of F-GRAND with $\beta = 1$. In line with (Chamberlain et al., 2021c), we examine two F-GRAND variants: F-GRAND-l (7) and F-GRAND-nl (9). Graph rewiring is not explored in this study. Where available, results from the paper (Chamberlain et al., 2021c) are used.

Performance. The results for graph node classification are summarized in Table 1, which also report the optimal β obtained via hyperparameter tuning. Consistent with our expectations, F-GRAND surpasses GRAND across nearly all datasets, given that GRAND represents a special case of FROND with $\beta = 1$. This underscores the consistent performance enhancement offered by the integration of memorized dynamics. This advantage is particularly noticeable on tree-structured datasets such as Airports and Disease, where F-GRAND markedly outperforms the baselines. For instance, F-GRAND-l outperforms both GRAND and GIL by approximately 7% on the Airport dataset. Interestingly,

our experiments indicate a smaller β (signifying greater dynamic memory) is preferable for such fractal-structured datasets, aligning with previous studies on fractional differential equations in biological and chemical systems (Nigmatullin, 1986; Mandelbrot & Mandelbrot, 1982; Ionescu et al., 2017). We refer readers to Section 4.4 for more analysis of β. Supporting our intuition with evidence, we evaluated graph datasets' fractal dimensions using Compact-Box-Burning (Song et al., 2007), and compared it to the optimal β, fractal dimension, and δ-hyperbolicity (as referenced in (Chami et al., 2019) for assessing tree-like structures—with lower values suggesting more tree-like graphs) as outlined in Table 18. Notably, we discerned a trend: a larger fractal dimension typically corresponds to a smaller optimal β. This observation strengthens our initial hypothesis in Section 1 that there exists some relationship between the fractal dimension and the order of the fractional dynamics.

4.2 Graph Classification of F-GRAND

We employ the Fake-NewsNet datasets (Dou et al., 2021), constructed from Politifact and Gossipcop fact-checking data. More details can be found in the Appendix D.2. This dataset features three types of node features: 768-dimensional BERT features, and 300-dimensional spaCy features, both extracted using pre-trained models, and 10-dimensional profile features from Twitter accounts. The graphs in the dataset exhibit a hierarchical tree structure. From Table 2, we observe that F-GRAND consistently outperforms GRAND with a notable edge on the POL dataset.

4.3 Oversmoothing of F-GRAND

To validate that F-GRAND mitigates the oversmoothing issue and performs well with numerous layers, we conducted an experiment using the basic predictor in the *Adams Bashforth Moulton* method as defined in (18). This allows us to generate architectures of varying depths. In this context, we utilize the fixed data splitting as described in (Chami et al., 2019). As illustrated in Fig. 2, optimal performance on the Cora dataset is attained with a network depth of 64 layers. When compared to GRAND-l, F-GRAND-l maintains a consistent performance level across all datasets as the number of layers increases, with virtually no performance drop observed up to 128 layers. This observation is consistent with our expectations, given that Theorem 2 predicts a slow algebraic convergence. In contrast, GRAND exhibits a faster rate of performance degradation particularly on the Airport dataset. Further details on oversmoothing mitigation are in Appendix D.7.

4.4 Ablation Study: Selection of β

In Table 3, we investigate the influence of β across various graph datasets. Notably, for the Cora dataset, a larger β is optimal, whereas, for tree-structured data, a smaller β is preferable. This suggests that the quantity of memorized dynamics should be tailored to the dataset's topology, and a default setting of memoryless graph diffusion with $\beta = 1$ may not be optimal. More comprehensive details concerning the variations in β can be found in the appendix, specifically in Table 15.

4.5 More integer-order continuous GNNs in FROND framework

Our FROND framework can be seamlessly applied to various other integer-order continuous GNNs, as elaborated in Appendix E. Specifically, we outline the node classification results of FROND based on the CDE model in Table 4. It is evident from the results that F-CDE enhances the performance of the CDE model across almost all **large heterophilic datasets.** The optimal β is determined through hyperparameter tuning. When $\beta = 1$, F-CDE seamlessly reverts to CDE, and the results from the original paper are reported. Additionally, we conduct comprehensive experiments detailed in Appendix E. The results for F-GRAND++, F-GREAD, and F-GraphCON are available in Table 19, Table 23, and Table 25, respectively. Collectively, these results demonstrate that our FROND framework can significantly bolster the performance of integer-order continuous GNNs, without introducing any additional training parameters to the backbone integer-order continuous GNNs.

Table 4: Node classification accuracy(%) of large heterophilic datasets

Model	Roman-empire	Wiki-cooc	Minesweeper	Questions	Workers	Amazon-ratings
CDE	91.64±0.28	97.99±0.38	95.50±5.23	75.17±0.99	80.70±1.04	47.63±0.43
F-CDE	**93.06±0.55**	**98.73±0.68**	**96.04±0.25**	75.17±0.99	**82.68±0.86**	**49.01±0.56**
β for F-CDE	0.9	0.6	0.6	1.0	0.4	0.1

5 Conclusion

We have introduced FROND, a novel graph learning framework that incorporates Caputo fractional derivatives to capture long-term memory in the graph feature updating dynamics. This approach has demonstrated superior performance compared to various traditional integer-order continuous GNNs. The resulting framework represents a significant advancement in graph representation learning, addressing key challenges in the field, such as oversmoothing. Our results highlight the potential of fractional calculus in enabling more effective graph learning algorithms.

ACKNOWLEDGMENTS AND DISCLOSURE OF FUNDING

This research is supported by the Singapore Ministry of Education Academic Research Fund Tier 2 grant MOE-T2EP20220-0002, and the National Research Foundation, Singapore and Infocomm Media Development Authority under its Future Communications Research and Development Programme. The computational work for this article was partially performed on resources of the National Supercomputing Centre, Singapore (https://www.nscc.sg). Xuhao Li is supported by the National Natural Science Foundation of China (Grant No. 12301491) and the Anhui Provincial Natural Science Foundation (Grant No. 2208085QA02).

REFERENCES

Ricardo Almeida, Nuno RO Bastos, and M Teresa T Monteiro. Modeling some real phenomena by fractional differential equations. *Mathematical Methods in the Applied Sciences*, 39(16): 4846–4855, 2016.

Uri Alon and Eran Yahav. On the bottleneck of graph neural networks and its practical implications. In *Proc. Int. Conf. Learn. Representations*, 2021.

Harbir Antil, Ratna Khatri, Rainald Löhner, and Deepanshu Verma. Fractional deep neural network via constrained optimization. *Mach. Learn.: Sci. Technol.*, 2(1):015003, 2020.

Haitham Ashoor, Xiaowen Chen, Wojciech Rosikiewicz, Jiahui Wang, Albert Cheng, Ping Wang, Yijun Ruan, and Sheng Li. Graph embedding and unsupervised learning predict genomic sub-compartments from hic chromatin interaction data. *Nat. Commun.*, 11, 2020.

Kendall Atkinson, Weimin Han, and David E Stewart. *Numerical solution of ordinary differential equations*. John Wiley & Sons, 2011.

Pedro HC Avelar, Anderson R Tavares, Marco Gori, and Luis C Lamb. Discrete and continuous deep residual learning over graphs. *arXiv preprint arXiv:1911.09554*, 2019.

Ronald L Bagley and PJ Torvik. A theoretical basis for the application of fractional calculus to viscoelasticity. *J. Rheology*, 27(3):201–210, 1983.

Deyu Bo, Xiao Wang, Chuan Shi, and Huawei Shen. Beyond low-frequency information in graph convolutional networks. In *Proceedings of the AAAI Conference on Artificial Intelligence*, volume 35, pp. 3950–3957, 2021.

Cristian Bodnar, Francesco Di Giovanni, Benjamin Paul Chamberlain, Pietro Liò, and Michael M. Bronstein. Neural sheaf diffusion: A topological perspective on heterophily and oversmoothing in GNNs. In *Advances Neural Inf. Process. Syst.*, 2022.

Dirk Brockmann, Lars Hufnagel, and Theo Geisel. The scaling laws of human travel. *Nature*, 439 (7075):462–465, 2006.

Ben Chamberlain, James Rowbottom, Maria I Gorinova, Michael Bronstein, Stefan Webb, and Emanuele Rossi. Grand: Graph neural diffusion. In *Proc. Int. Conf. Mach. Learn.*, pp. 1407–1418, 2021a.

Benjamin Chamberlain, James Rowbottom, Davide Eynard, Francesco Di Giovanni, Xiaowen Dong, and Michael Bronstein. Beltrami flow and neural diffusion on graphs. In *Advances Neural Inf. Process. Syst.*, pp. 1594–1609, 2021b.

Benjamin Paul Chamberlain, James Rowbottom, Maria Goronova, Stefan Webb, Emanuele Rossi, and Michael M Bronstein. Grand: Graph neural diffusion. In *Proc. Int. Conf. Mach. Learn.*, 2021c.

Ines Chami, Zhitao Ying, Christopher Ré, and Jure Leskovec. Hyperbolic graph convolutional neural networks. In *Advances Neural Inf. Process. Syst.*, 2019.

Jinyin Chen, Yangyang Wu, Xuanheng Xu, Yixian Chen, Haibin Zheng, and Qi Xuan. Fast gradient attack on network embedding. *ArXiv*, 2018a.

Ming Chen, Zhewei Wei, Zengfeng Huang, Bolin Ding, and Yaliang Li. Simple and deep graph convolutional networks. In *Proc. Int. Conf. Mach. Learn.*, pp. 1725–1735, 2020.

Ricky TQ Chen, Yulia Rubanova, Jesse Bettencourt, and David Duvenaud. Neural ordinary differential equations. In *Advances Neural Inf. Process. Syst.*, 2018b.

Eli Chien, Jianhao Peng, Pan Li, and Olgica Milenkovic. Adaptive universal generalized pagerank graph neural network. *arXiv preprint arXiv:2006.07988*, 2020.

Jeongwhan Choi, Seoyoung Hong, Noseong Park, and Sung-Bae Cho. Gread: Graph neural reaction-diffusion networks. In *Proc. Int. Conf. Mach. Learn.*, 2023.

Fan RK Chung. *Spectral graph theory*, volume 92. American Mathematical Soc., 1997.

Alan M. Cohen. *Inversion Formulae and Practical Results*, pp. 23–44. Springer US, Boston, MA, 2007.

Bernard D Coleman and Walter Noll. Foundations of linear viscoelasticity. *Rev. Modern Phys.*, 33 (2):239, 1961.

Weihua Deng. Short memory principle and a predictor–corrector approach for fractional differential equations. *J. Comput. Appl. Math.*, 206(1):174–188, 2007.

Francesco Di Giovanni, James Rowbottom, Benjamin P Chamberlain, Thomas Markovich, and Michael M Bronstein. Graph neural networks as gradient flows. *arXiv preprint arXiv:2206.10991*, 2022.

Francesco Di Giovanni, James Rowbottom, Benjamin Paul Chamberlain, Thomas Markovich, and Michael M Bronstein. Understanding convolution on graphs via energies. *Tran. Mach. Learn. Res.*, 2023.

Fernando Diaz-Diaz and Ernesto Estrada. Time and space generalized diffusion equation on graph/networks. *Chaos, Solitons and Fractals*, 156:111791, 2022.

Kai Diethelm. *The analysis of fractional differential equations: an application-oriented exposition using differential operators of Caputo type*, volume 2004. Springer, 2010.

Kai Diethelm and Neville J Ford. Analysis of fractional differential equations. *J. Math. Anal. Appl.*, 265(2):229–248, 2002.

Kai Diethelm, Neville J Ford, and Alan D Freed. Detailed error analysis for a fractional adams method. *Numer. Algorithms*, 36:31–52, 2004.

Yingtong Dou, Kai Shu, Congying Xia, Philip S. Yu, and Lichao Sun. User preference-aware fake news detection. In *Proc. Int. ACM SIGIR Conf. Res. Develop. Inform. Retrieval*, 2021.

Jian Du, Shanghang Zhang, Guanhang Wu, José M. F. Moura, and Soummya Kar. Topology adaptive graph convolutional networks. *ArXiv*, abs/1710.10370, 2017.

Lun Du, Xiaozhou Shi, Qiang Fu, Xiaojun Ma, Hengyu Liu, Shi Han, and Dongmei Zhang. Gbk-gnn: Gated bi-kernel graph neural networks for modeling both homophily and heterophily. In *Proceedings of the ACM Web Conference 2022*, pp. 1550–1558, 2022.

Emilien Dupont, Arnaud Doucet, and Yee Whye Teh. Augmented neural odes. In *Advances Neural Inf. Process. Syst.*, pp. 1–11, 2019.

Rick Durrett. *Probability: theory and examples*, volume 49. Cambridge university press, 2019.

Jiarui Feng, Yixin Chen, Fuhai Li, Anindya Sarkar, and Muhan Zhang. How powerful are k-hop message passing graph neural networks. *Advances in Neural Information Processing Systems*, 35: 4776–4790, 2022.

Guang-hua Gao and Zhi-zhong Sun. A compact finite difference scheme for the fractional sub-diffusion equations. *Journal of Computational Physics*, 230(3):586–595, 2011.

Hongyang Gao and Shuiwang Ji. Graph u-nets. In *Proc. Int. Conf. Mach. Learn.*, pp. 2083–2092, 2019.

José Francisco Gómez-Aguilar, Margarita Miranda-Hernández, MG López-López, Victor Manuel Alvarado-Martínez, and Dumitru Baleanu. Modeling and simulation of the fractional space-time diffusion equation. *Commun. Nonlinear Sci. Numer. Simul.*, 30(1-3):115–127, 2016.

Rudolf Gorenflo and Francesco Mainardi. Fractional diffusion processes: probability distributions and continuous time random walk. In *Process. Long-Range Correlations: Theory Appl.*, pp. 148–166. Springer, 2003.

Rudolf Gorenflo, Francesco Mainardi, Daniele Moretti, and Paolo Paradisi. Time fractional diffusion: a discrete random walk approach. *Nonlinear Dynamics*, 29:129–143, 2002.

Alessio Gravina, Davide Bacciu, and Claudio Gallicchio. Anti-symmetric dgn: A stable architecture for deep graph networks. In *Proc. Int. Conf. Learn. Representations*, 2022.

Ling Guo, Hao Wu, Xiaochen Yu, and Tao Zhou. Monte carlo fpinns: Deep learning method for forward and inverse problems involving high dimensional fractional partial differential equations. *Comput. Methods Appl. Mechanics Eng.*, 400:115523, 2022.

Kyle B Gustafson, Basil S Bayati, and Philip A Eckhoff. Fractional diffusion emulates a human mobility network during a simulated disease outbreak. *Frontiers Ecology Evol.*, 5:35, 2017.

Benjamin Gutteridge, Xiaowen Dong, Michael M Bronstein, and Francesco Di Giovanni. Drew: Dynamically rewired message passing with delay. In *Proc. Int. Conf. Mach. Learn.*, pp. 12252–12267, 2023.

Eldad Haber and Lars Ruthotto. Stable architectures for deep neural networks. *Inverse Problems*, 34 (1):1–23, December 2017.

William L. Hamilton, Rex Ying, and Jure Leskovec. Inductive representation learning on large graphs. In *Advances Neural Inf. Process. Syst.*, 2017.

Philip Hartman. *Ordinary differential equations*. SIAM, 2002.

Kaiming He, Xiangyu Zhang, Shaoqing Ren, and Jian Sun. Deep residual learning for image recognition. In *Proc. Conf. Comput. Vision Pattern Recognition*, 2016.

Roger A Horn and Charles R Johnson. *Matrix analysis*. Cambridge university press, New York, 2012.

Weihua Hu, Matthias Fey, Marinka Zitnik, Yuxiao Dong, Hongyu Ren, Bowen Liu, Michele Catasta, and Jure Leskovec. Open graph benchmark: Datasets for machine learning on graphs. *arXiv:2005.00687*, 2020.

Weihua Hu, Matthias Fey, Marinka Zitnik, Yuxiao Dong, Hongyu Ren, Bowen Liu, Michele Catasta, and Jure Leskovec. Open graph benchmark: Datasets for machine learning on graphs, 2021.

Gao Huang, Zhuang Liu, Laurens Van Der Maaten, and Kilian Q Weinberger. Densely connected convolutional networks. In *Proc. Conf. Comput. Vision Pattern Recognition*, 2017.

Hussain Hussain, Meng Cao, Sandipan Sikdar, Denis Helic, Elisabeth Lex, Markus Strohmaier, and Roman Kern. Adversarial inter-group link injection degrades the fairness of graph neural networks. *arXiv preprint arXiv:2209.05957*, 2022.

C Ionescu, A Lopes, Dana Copot, JA Tenreiro Machado, and Jason HT Bates. The role of fractional calculus in modeling biological phenomena: A review. *Commun. Nonlinear Sci. Numer. Simul.*, 51:141–159, 2017.

Rana Javadi, Hamid Mesgarani, Omid Nikan, and Zakieh Avazzadeh. Solving fractional order differential equations by using fractional radial basis function neural network. *Symmetry*, 15(6): 1275, 2023.

Bangti Jin, Buyang Li, and Zhi Zhou. Correction of high-order bdf convolution quadrature for fractional evolution equations. *SIAM J. Sci. Comput.*, 39(6):A3129–A3152, 2017.

Wei Jin, Yao Ma, Xiaorui Liu, Xianfeng Tang, Suhang Wang, and Jiliang Tang. Graph structure learning for robust graph neural networks. In *Proc. Int. Conf. Knowl. Discovery Data Mining*, pp. 66–74, 2020.

Qiyu Kang, Kai Zhao, Yang Song, Sijie Wang, and Wee Peng Tay. Node embedding from neural Hamiltonian orbits in graph neural networks. In *Proc. International Conference on Machine Learning*, pp. 15786–15808, 2023.

JS Kim, K-I Goh, G Salvi, E Oh, B Kahng, and D Kim. Fractality in complex networks: Critical and supercritical skeletons. *Physical Review E*, 75(1):016110, 2007.

Diederik P Kingma and Jimmy Ba. Adam: A method for stochastic optimization. *arXiv preprint arXiv:1412.6980*, 2014.

Thomas N. Kipf and Max Welling. Semi-supervised classification with graph convolutional networks. In *Proc. Int. Conf. Learn. Representations*, 2017.

Granino Arthur Korn and Theresa M Korn. *Mathematical handbook for scientists and engineers: definitions, theorems, and formulas for reference and review*. Courier Corporation, 2000.

Diego Krapf. Mechanisms underlying anomalous diffusion in the plasma membrane. *Current Topics Membranes*, 75:167–207, 2015.

Guohao Li, Matthias Muller, Ali Thabet, and Bernard Ghanem. Deepgcns: Can gcns go as deep as cnns? In *Proc. Int. Conf. Learn. Representations*, pp. 9267–9276, 2019.

Guohao Li, Chenxin Xiong, Ali Thabet, and Bernard Ghanem. Deepergcn: All you need to train deeper gcns. *arXiv preprint arXiv:2006.07739*, 2020a.

Xiang Li, Renyu Zhu, Yao Cheng, Caihua Shan, Siqiang Luo, Dongsheng Li, and Weining Qian. Finding global homophily in graph neural networks when meeting heterophily. In *International Conference on Machine Learning*, pp. 13242–13256. PMLR, 2022.

Yaxin Li, Wei Jin, Han Xu, and Jiliang Tang. Deeprobust: A pytorch library for adversarial attacks and defenses. *arXiv preprint arXiv:2005.06149*, 2020b.

Derek Lim, Felix Hohne, Xiuyu Li, Sijia Linda Huang, Vaishnavi Gupta, Omkar Bhalerao, and Ser Nam Lim. Large scale learning on non-homophilous graphs: New benchmarks and strong simple methods. *Advances in Neural Information Processing Systems*, 34:20887–20902, 2021.

Zijian Liu, Yaning Wang, Yang Luo, and Chunbo Luo. A regularized graph neural network based on approximate fractional order gradients. *Mathematics*, 10(8):1320, 2022.

Sitao Luan, Chenqing Hua, Qincheng Lu, Jiaqi Zhu, Mingde Zhao, Shuyuan Zhang, Xiao-Wen Chang, and Doina Precup. Revisiting heterophily for graph neural networks. *Advances in neural information processing systems*, 35:1362–1375, 2022.

Chunwan Lv and Chuanju Xu. Error analysis of a high order method for time-fractional diffusion equations. *SIAM J. Sci. Comput.*, 38(5):A2699–A2724, 2016.

J Tenreiro Machado, Virginia Kiryakova, and Francesco Mainardi. Recent history of fractional calculus. *Communications in nonlinear science and numerical simulation*, 16(3):1140–1153, 2011.

F. Mainardi. On some properties of the mittag-leffler function $\mathbf{E}_\alpha(-\mathbf{t}^\alpha)$, completely monotone for $\mathbf{t} > \mathbf{0}$ with $\mathbf{0} < \alpha < \mathbf{1}$. *Discrete Continuous Dyn. Syst. Ser. B*, 19(7):2267–2278, 2014.

Benoit B Mandelbrot and Benoit B Mandelbrot. *The fractal geometry of nature*, volume 1. WH freeman New York, 1982.

Sohir Maskey, Raffaele Paolino, Aras Bacho, and Gitta Kutyniok. A fractional graph laplacian approach to oversmoothing. *arXiv preprint arXiv:2305.13084*, 2023.

Barry R Masters. Fractal analysis of the vascular tree in the human retina. *Annu. Rev. Biomed. Eng.*, 6:427–452, 2004.

Julian McAuley, Christopher Targett, Qinfeng Shi, and Anton van den Hengel. Image-based recommendations on styles and substitutes. In *Proc. Int. ACM SIGIR Conf. Res. Develop. Inform. Retrieval*, pp. 43–52, 2015.

Andrew McCallum, Kamal Nigam, Jason D. M. Rennie, and Kristie Seymore. Automating the construction of internet portals with machine learning. *Inf. Retrieval*, 3:127–163, 2004.

Federico Monti, Davide Boscaini, Jonathan Masci, Emanuele Rodola, Jan Svoboda, and Michael M Bronstein. Geometric deep learning on graphs and manifolds using mixture model cnns. In *Proc. Conf. Comput. Vision Pattern Recognition*, pp. 5115–5124, 2017.

Galileo Mark Namata, Ben London, Lise Getoor, and Bert Huang. Query-driven active surveying for collective classification. In *Workshop Mining Learn. Graphs*, 2012.

Ravil'Rashidovich Nigmatullin. Fractional integral and its physical interpretation. *Theoretical and Mathematical Physics*, 90(3):242–251, 1992.

RR Nigmatullin. The realization of the generalized transfer equation in a medium with fractal geometry. *Physica status solidi (b)*, 133(1):425–430, 1986.

Bachmann–Landau Order Notations. Big o notation, 2023. URL `https://en.wikipedia.org/wiki/Big_O_notation`. Accessed: Sep 1, 2023.

Kenta Oono and Taiji Suzuki. Graph neural networks exponentially lose expressive power for node classification. In *Proc. Int. Conf. Learn. Representations*, 2020.

Guofei Pang, Lu Lu, and George Em Karniadakis. fpinns: Fractional physics-informed neural networks. *SIAM J. Sci. Comput.*, 41(4):A2603–A2626, 2019.

Adam Paszke, Sam Gross, Soumith Chintala, Gregory Chanan, Edward Yang, Zachary DeVito, Zeming Lin, Alban Desmaison, Luca Antiga, and Adam Lerer. Automatic differentiation in pytorch. In *Advances Neural Inf. Process. Syst.*, 2017.

Hongbin Pei, Bingzhe Wei, Kevin Chen-Chuan Chang, Yu Lei, and Bo Yang. Geom-gcn: Geometric graph convolutional networks. *arXiv preprint arXiv:2002.05287*, 2020.

Igor Podlubny. Fractional-order systems and fractional-order controllers. *Institute of Experimental Physics, Slovak Academy of Sciences, Kosice*, 12(3):1–18, 1994.

Igor Podlubny. *Fractional Differential Equations*. Academic Press, 1999.

Michael Poli, Stefano Massaroli, Junyoung Park, Atsushi Yamashita, Hajime Asama, and Jinkyoo Park. Graph neural ordinary differential equations. *arXiv preprint arXiv:1911.07532*, 2019.

Alessio Quaglino, Marco Gallieri, Jonathan Masci, and Jan Koutník. Snode: Spectral discretization of neural odes for system identification. In *Proc. Int. Conf. Learn. Representations*, 2019.

Ahmed Gomaa Radwan, Ahmed S Elwakil, and Ahmed M Soliman. Fractional-order sinusoidal oscillators: design procedure and practical examples. *IEEE Tran. Circuits and Syst.*, 55(7): 2051–2063, 2008.

T Konstantin Rusch, Ben Chamberlain, James Rowbottom, Siddhartha Mishra, and Michael Bronstein. Graph-coupled oscillator networks. In *Proc. Int. Conf. Mach. Learn.*, 2022.

Enrico Scalas, Rudolf Gorenflo, and Francesco Mainardi. Fractional calculus and continuous-time finance. *Physica A: Statistical Mechanics and its Applications*, 284(1-4):376–384, 2000.

Prithviraj Sen, Galileo Namata, Mustafa Bilgic, Lise Getoor, Brian Galligher, and Tina Eliassi-Rad. Collective classification in network data. *AI Magazine*, 29(3):93, Sep. 2008.

Oleksandr Shchur, Maximilian Mumme, Aleksandar Bojchevski, and Stephan Günnemann. Pitfalls of graph neural network evaluation. *Relational Representation Learning Workshop, Advances Neural Inf. Process. Syst.,*, 2018.

Chaoming Song, Shlomo Havlin, and Hernan A Makse. Self-similarity of complex networks. *Nature*, 433(7024):392–395, 2005.

Chaoming Song, Lazaros K Gallos, Shlomo Havlin, and Hernán A Makse. How to calculate the fractal dimension of a complex network: the box covering algorithm. *J. Stat. Mech. Theory Exp.*, 2007(03):P03006, 2007.

Yang Song, Qiyu Kang, Sijie Wang, Kai Zhao, and Wee Peng Tay. On the robustness of graph neural diffusion to topology perturbations. In *Advances Neural Inf. Process. Syst.*, 2022.

Didier Sornette. *Critical phenomena in natural sciences: chaos, fractals, selforganization and disorder: concepts and tools*. Springer Science & Business Media, 2006.

Zhi-zhong Sun and Xiaonan Wu. A fully discrete difference scheme for a diffusion-wave system. *Applied Numerical Mathematics*, 56(2):193–209, 2006.

Vasily E Tarasov. *Fractional dynamics: applications of fractional calculus to dynamics of particles, fields and media*. Springer Science & Business Media, 2011.

Matthew Thorpe, Hedi Xia, Tan Nguyen, Thomas Strohmer, Andrea Bertozzi, Stanley Osher, and Bao Wang. Grand++: Graph neural diffusion with a source term. In *Proc. Int. Conf. Learn. Representations*, 2022.

WenYi Tian, Han Zhou, and Weihua Deng. A class of second order difference approximations for solving space fractional diffusion equations. *Math. Comput.*, 84(294):1703–1727, 2015.

Ashish Vaswani, Noam Shazeer, Niki Parmar, Jakob Uszkoreit, Llion Jones, Aidan N Gomez, Łukasz Kaiser, and Illia Polosukhin. Attention is all you need. *Advances in neural information processing systems*, 30, 2017.

Petar Veličković, Guillem Cucurull, Arantxa Casanova, Adriana Romero, Pietro Liò, and Yoshua Bengio. Graph attention networks. In *Proc. Int. Conf. Learn. Representations*, pp. 1–12, 2018.

Jihong Wang, Minnan Luo, Fnu Suya, Jundong Li, Zijiang Yang, and Qinghua Zheng. Scalable attack on graph data by injecting vicious nodes. *Data Mining Knowl. Discovery*, pp. 1 – 27, 2020.

Shupeng Wang, Hui Zhang, and Xiaoyun Jiang. Fractional physics-informed neural networks for time-fractional phase field models. *Nonlinear Dyn.*, 110(3):2715–2739, 2022a.

Yuelin Wang, Kai Yi, Xinliang Liu, Yu Guang Wang, and Shi Jin. Acmp: Allen-cahn message passing with attractive and repulsive forces for graph neural networks. In *Proc. Int. Conf. Learn. Representations*, 2022b.

Marcin Waniek, Tomasz P. Michalak, Michael J. Wooldridge, and Talal Rahwan. Hiding individuals and communities in a social network. *Nature Human Behaviour*, 2(1):139–147, 2018.

Ee Weinan. A proposal on machine learning via dynamical systems. *Commun. Math. Statist.*, 1(5): 1–11, 2017.

Wikipedia. Hardy–littlewood tauberian theorem, 2023. URL `https://en.wikipedia.org/wiki/Hardy%E2%80%93Littlewood_Tauberian_theorem`. Accessed: Sep 1, 2023.

Zonghan Wu, Shirui Pan, Fengwen Chen, Guodong Long, Chengqi Zhang, and Philip S. Yu. A comprehensive survey on graph neural networks. *IEEE Trans. Neural Netw. Learn. Syst.*, 32(1): 4–24, 2021.

Louis-Pascal Xhonneux, Meng Qu, and Jian Tang. Continuous graph neural networks. In *Proc. Int. Conf. Mach. Learn.*, pp. 10432–10441, 2020.

Keyulu Xu, Chengtao Li, Yonglong Tian, Tomohiro Sonobe, Ken-ichi Kawarabayashi, and Stefanie Jegelka. Representation learning on graphs with jumping knowledge networks. In *Proc. Int. Conf. Mach. Learn.*, pp. 5453–5462, 2018.

Hanshu Yan, Jiawei Du, Vincent YF Tan, and Jiashi Feng. On robustness of neural ordinary differential equations. In *Advances Neural Inf. Process. Syst.*, pp. 1–13, 2018.

Yujun Yan, Milad Hashemi, Kevin Swersky, Yaoqing Yang, and Danai Koutra. Two sides of the same coin: Heterophily and oversmoothing in graph convolutional neural networks. In *2022 IEEE International Conference on Data Mining (ICDM)*, pp. 1287–1292. IEEE, 2022.

Xiang Yue, Zhen Wang, Jingong Huang, Srinivasan Parthasarathy, Soheil Moosavinasab, Yungui Huang, Simon M Lin, Wen Zhang, Ping Zhang, and Huan Sun. Graph embedding on biomedical networks: methods, applications and evaluations. *Bioinformatics*, 36(4):1241–1251, 2019.

Santos B Yuste and Luis Acedo. An explicit finite difference method and a new von neumann-type stability analysis for fractional diffusion equations. *SIAM Journal on Numerical Analysis*, 42(5): 1862–1874, 2005.

Hanqing Zeng, Hongkuan Zhou, Ajitesh Srivastava, Rajgopal Kannan, and Viktor Prasanna. Graph-saint: Graph sampling based inductive learning method, 2020.

Ziwei Zhang, Peng Cui, and Wenwu Zhu. Deep learning on graphs: A survey. *IEEE Trans. Knowl. Data Eng.*, 34(1):249–270, Jan 2022.

Kai Zhao, Qiyu Kang, Yang Song, Rui She, Sijie Wang, and Wee Peng Tay. Graph neural convection-diffusion with heterophily. In *Proc. Inter. Joint Conf. Artificial Intell.*, Macao, China, 2023.

Qinkai Zheng, Yixiao Fei, Yanhao Li, Qingmin Liu, Minhao Hu, and Qibo Sun. Kdd cup 2020 ml track 2 adversarial attacks and defense on academic graph 1st place solution, 2022. URL `https://github.com/Stanislas0/KDD_CUP_2020_MLTrack2_SPEIT`. Accessed: May 1, 2022.

Jiong Zhu, Yujun Yan, Lingxiao Zhao, Mark Heimann, Leman Akoglu, and Danai Koutra. Beyond homophily in graph neural networks: Current limitations and effective designs. *Advances in neural information processing systems*, 33:7793–7804, 2020a.

Jiong Zhu, Ryan A Rossi, Anup Rao, Tung Mai, Nedim Lipka, Nesreen K Ahmed, and Danai Koutra. Graph neural networks with heterophily. In *Proceedings of the AAAI conference on artificial intelligence*, volume 35, pp. 11168–11176, 2021.

Shichao Zhu, Shirui Pan, Chuan Zhou, Jia Wu, Yanan Cao, and Bin Wang. Graph geometry interaction learning. In *Advances Neural Inf. Process. Syst.*, 2020b.

Juntang Zhuang, Nicha Dvornek, Xiaoxiao Li, and James S Duncan. Ordinary differential equations on graph networks. 2019.

Xu Zou, Qinkai Zheng, Yuxiao Dong, Xinyu Guan, Evgeny Kharlamov, Jialiang Lu, and Jie Tang. Tdgia: Effective injection attacks on graph neural networks. In *Proc. Int. Conf. Knowl. Discovery Data Mining*, pp. 2461–2471, 2021.

Daniel Zügner and Stephan Günnemann. Adversarial attacks on graph neural networks via meta learning. In *Proc. Int. Conf. Learn. Representations*, 2019.

Daniel Zügner, Amir Akbarnejad, and Stephan Günnemann. Adversarial attacks on neural networks for graph data. In *Proc. Int. Conf. Knowl. Discovery Data Mining*, 2018.

This appendix complements the main body of our paper, providing additional details and supporting evidence for the assertions made therein. The structure of this document is as follows:

1. We discuss related work in Appendix A.
2. We offer a concise review of fractional calculus in Appendix B.
3. We include more solver details and variants in Appendix C.
4. We present dataset statistics, experimental settings, and additional experimental results in Appendix D.
5. We introduce more dynamics within the FROND framework in Appendix E.
6. We provide proofs for all theoretical assertions made in the main paper in Appendix F.
7. We discuss the limitations of our work and its broader impact in the final section of this supplementary material.

A Related Work

Fractional Calculus and Its Applications

The field of fractional calculus has seen a notable surge in interest recently due to its wide-ranging applications across various domains. These include, but are not limited to, numerical analysis (Yuste & Acedo, 2005), viscoelastic materials (Coleman & Noll, 1961), population growth models (Almeida et al., 2016), control theory (Podlubny, 1994), signal processing (Machado et al., 2011), financial mathematics (Scalas et al., 2000), and particularly in the representation of porous and fractal phenomena (Nigmatullin, 1986; Mandelbrot & Mandelbrot, 1982; Ionescu et al., 2017). Within these contexts, fractional-order differential equations have been developed as a powerful extension to the conventional integer-ordered differential equations, offering a resilient mathematical framework for system analysis (Diethelm & Ford, 2002). To illustrate, in studies related to diffusion processes, researchers have utilized fractional calculus for delineating various natural and synthetic systems, from protein diffusion in cellular membranes (Krapf, 2015), to animal migration patterns (Brockmann et al., 2006), human mobility networks (Gustafson et al., 2017), and even biological phenomena pertinent to respiratory tissues and neuroscience (Ionescu et al., 2017). Interestingly, the occurrence of subdiffusion, as modelled by time-fractional differential equations, has been observed in scenarios where diffusing entities encounter intermittent obstructions due to the complex geometrical structure or interaction dynamics of the environment (Diaz-Diaz & Estrada, 2022; Sornette, 2006).

Within the realm of deep learning, (Liu et al., 2022) proposes a novel approach to GNN parameter optimization using the fractional derivative. This marks a significant shift from the conventional integer-order derivative employed in optimization algorithms like SGD or Adam (Kingma & Ba, 2014) with respect to the weights. The essence of their work fundamentally differs from ours, which focuses on the fractional-derivative evolution of node embeddings, not gradient optimization. A detailed examination of the study by (Liu et al., 2022) is pivotal as it adopts fractional derivatives instead of the standard first-order derivatives *during the weight updating phase of a GNN in the gradient descent.* Specifically, attention is drawn to equation (16) in (Liu et al., 2022), elucidating that the fractional derivative is operational on the loss function. This stands in stark contrast to the FROND framework proposed in this work. As delineated in equation (6) of our paper, the fractional derivative is applied to the evolving node feature, representing an implementation of a fractional-order feature updating process, thereby showcasing a clear distinction in the application of fractional derivatives.

Additionally, (Antil et al., 2020) incorporates insights from fractional calculus and its L1 approximation of the fractional derivative to craft a densely connected neural network. Their aim is to adeptly handle non-smooth data and counteract the vanishing gradient problem. While our research operates within a similar sphere, we have introduced fractional calculus into integer-order continuous GNNs. Our work examines the potential of fractional derivatives in node embedding evolution to address the oversmoothing issue and establishes a connection to non-Markovian dynamic processes. Our framework paves the way for a new class of GNNs, enabling a wide spectrum of learnable feature-updating processes influenced by memory effects.

From the perspective of physics-informed machine learning, another line of research is dedicated to crafting neural networks rooted in physical laws to solve fractional PDEs. A pioneering work

in this domain is the Fractional Physics Informed Neural Networks (fPINNs) (Pang et al., 2019). Subsequent research, such as (Guo et al., 2022; Javadi et al., 2023; Wang et al., 2022a), has evolved in this direction. It is worth noting that this line of research is starkly different from our problem formulation.

Integer-Order Continuous GNNs

Recent research has illuminated a fascinating intersection between differential equations and neural networks. The concept of continuous dynamical systems as a framework for deep learning has been initially explored by (Weinan, 2017). The seminal work of (Chen et al., 2018b) introduces neural ODEs with open-source solvers to model continuous residual layers, which has subsequently been applied to the field of GNNs. By utilizing neural ODEs, we can align the inputs and outputs of a neural network with specific physical laws, enhancing the network's explainability (Weinan, 2017; Chamberlain et al., 2021c). Additionally, separate advancements in this domain have led to improvements in neural network performance (Dupont et al., 2019), robustness(Yan et al., 2018), and gradient stability (Haber & Ruthotto, 2017; Gravina et al., 2022). In a similar vein, (Avelar et al., 2019) models continuous residual layers in GCN, leveraging neural ODE solvers to produce output. Further, the work of (Poli et al., 2019) proposes a model that considers a continuum of GNN layers, merging discrete topological structures and differential equations in a manner compatible with various static and autoregressive GNN models. The study (Zhuang et al., 2019) introduces GODE, which enables the modeling of continuous diffusion processes on graphs. It also suggests that the oversmoothing issue in GNNs may be associated with the asymptotic stability of ODEs. Recently, GraphCON (Rusch et al., 2022) adopts the coupled oscillator model that preserves the graph's Dirichlet energy over time and mitigates the oversmoothing problem. In (Chamberlain et al., 2021a), the authors modeled information propagation as a diffusion process of a substance from regions of higher to lower concentration. The Beltrami diffusion model is utilized in (Chamberlain et al., 2021b; Song et al., 2022) to enhance rewiring and improve the robustness of the graph. The study by (Bodnar et al., 2022) introduces general sheaf diffusion operators to regulate the diffusion process and maintain non-smoothness in heterophilic graphs, leading to improved node classification performance. Meanwhile, ACMP (Wang et al., 2022b) is inspired by particle reaction-diffusion processes, taking into account repulsive and attractive force interactions between particles. Concurrently, the graph CDE model (Zhao et al., 2023) is crafted to handle heterophilic graphs and is inspired by the convection-diffusion process. GRAND++ (Thorpe et al., 2022) leverages heat diffusion with sources to train models effectively with a limited amount of labeled training data. Concurrently, GREAD (Choi et al., 2023) articulates a GNN approach, which is premised on reaction-diffusion equations, aiming to negotiate heterophilic datasets effectively. In another development, the continuous GNN as an ODE (Maskey et al., 2023) encapsulates a graph spatial domain rewiring, leveraging the fractional order of the graph Laplacian matrix, presenting a substantial advancement in understanding graph structures.

Our FROND extends the above integer-order continuous GNNs by incorporating the Caputo fractional derivative. The models mentioned can be reduced from our unified mathematical framework, with variations manifesting from the choice of the dynamic equation $\mathcal{F}(\mathbf{W}, \mathbf{X}(t))$ in (6) *and as β equals 1 in the fractional derivative operator D_t^β.*

Skip Connections in GNNs

The incorporation of skip or dense connections within network layers has been a transformative approach within deep learning literature. Initially popularized through the ResNet architecture (He et al., 2016), this strategy introduces shortcut pathways for gradient flow during backpropagation, thereby simplifying the training of more profound networks. While this architectural design has been instrumental in improving Convolutional Neural Networks (CNNs), it has also been employed in GNNs to bolster their representational capacity and mitigate the vanishing gradient problem. For example, the Graph U-Net (Gao & Ji, 2019) employs skip connections to enable efficient information propagation across layers. Similarly, the Jump Knowledge Network (Xu et al., 2018) implements a layer-aggregation mechanism that amalgamates outputs from all preceding layers, a strategy reminiscent of the dense connections found in DenseNet (Huang et al., 2017). Furthermore, the work (Chen et al., 2020) introduces GCNII, an extension of the standard GCN model that incorporates two simple techniques, initial residual and identity mapping, to tackle the oversmoothing problem. Expanding on the idea of depth in GNNs, (Li et al., 2019; 2020a) propose DeepGCNs, an innovative architecture that employs residual/dense connections along with dilated convolutions. By incorporating fractional-order dynamics and memory effects, we pave the way for a profound

understanding of those GNN architectures and the development of more adaptable and potent graph representation learning. The work (Di Giovanni et al., 2023) suggests that gradient-flow message passing neural networks may be able to deal with heterophilic graphs provided that a residual connection is available. The paper (Gutteridge et al., 2023) proposes a spatial domain rewiring and focuses on long-range interactions. DRew in (Gutteridge et al., 2023) does not adhere to any ODE evolutionary structure. Its numerical experiments are also done on the long-range graph benchmark, instead of the usual GNN benchmark datasets we have used in our paper. Additionally, the skip connection in the vDRew from (Gutteridge et al., 2023) specifically links an $n-k$-th layer to the n-th layer. This design is fundamentally different from our FDE approach. By incorporating fractional-order dynamics and memory effects into our framework, we not only provide a fresh perspective on understanding the structural design of skip connections in GNNs as a continuous dynamical process but also lay a foundation for the development of more versatile and powerful mechanisms for graph representation learning.

B Review of Caputo Time-Fractional Derivative

We appreciate the need for a more accessible explanation of the Caputo time-fractional derivative and its derivation, as the mathematical intricacies may be challenging for some readers in the GNN community. To address this, we are providing a more comprehensive background in this section. In the main paper, we briefly touched upon fractional calculus, with a particular focus on the *Caputo* fractional derivative that has been employed in our work. In this appendix, we aim to provide a more detailed overview of it and explain why it is widely employed in applications. We have based our FROND framework on the assumption that the solution to the fractional differential equation exists and is unique. The appendix provides explicit conditions for this, which are automatically satisfied in most neural network designs exhibiting local Lipschitz continuity. To simplify, these conditions are akin to those for ordinary differential equations, a common assumption implicitly made in integer-order continuous GNNs such as GRAND (Chamberlain et al., 2021c), GraphCON (Rusch et al., 2022), GRAND++ (Thorpe et al., 2022), GREAD (Choi et al., 2023) and CDE (Zhao et al., 2023).

B.1 Caputo Fractional Derivative and Its Compatibility of Integer-order Derivative

In the main paper, our focus is predominantly on the order $\beta \in (0, 1]$ for the sake of simplification. The Caputo fractional derivative of a function $f(t)$ over an interval $[0, b]$, of a general positive order $\beta \in (0, \infty)$, is defined as follows:

$$D_t^\beta f(t) = \frac{1}{\Gamma(\lceil\beta\rceil - \beta)} \int_0^t (t-\tau)^{\lceil\beta\rceil-\beta-1} f^{(\lceil\beta\rceil)}(\tau)\mathrm{d}\tau, \tag{19}$$

Here, $\lceil\beta\rceil$ is the smallest integer greater than or equal to β, $\Gamma(\cdot)$ denotes the gamma function, and $f^{(\lceil\beta\rceil)}(\cdot)$ denotes the $\lceil\beta\rceil$-order derivative of $f(\cdot)$. Within this definition, it is presumed that $f^{(\lceil\beta\rceil)} \in L^1[0, b]$, i.e., $f^{(\lceil\beta\rceil)}$ is Lebesgue integrable, to ensure the well-defined nature of $D_t^\beta f(t)$ as per (19) (Diethelm, 2010). For a vector-valued function, the Caputo fractional derivative is defined on a component-by-component basis for each dimension, similar to the integer-order derivative. For ease of exposition, we discuss only the scalar case here, although all the following results can be generalized to vector-valued functions. The Laplace transform for a general order $\beta \in (0, \infty)$ is presented in Theorem 7.1 (Diethelm, 2010) as:

$$\mathcal{L}D_t^\beta f(s) = s^\beta \mathcal{L}f(s) - \sum_{k=1}^{\lceil\beta\rceil} s^{\beta-k} f^{(k-1)}(0). \tag{20}$$

where we assume that the Laplace transform $\mathcal{L}f$ exists on $[s_0, \infty)$ for some $s_0 \in \mathbb{R}$. In contrast, for the integer-order derivative $f^{(\beta)}$ where β is a positive integer, we also have the formulation (20), with the only difference being the range of β. Therefore, as β approaches some integer, the Laplace transform of the Caputo fractional derivative converges to the Laplace transform of the traditional integer-order derivative. *As a result, we can conclude that the Caputo fractional derivative operator generalizes the traditional integer-order derivative since their Laplace transforms coincide when β takes an integer value.* The inverse Laplace transform specifies the uniquely determined $D_t^\beta f = f^{(\beta)}$ when β is an integer (in the sense of almost everywhere (Cohen, 2007)).

Under specific reasonable conditions, we can directly present this generalization as follows. Suppose $f^{(\lceil\beta\rceil)}(t)$ (19) is continuously differentiable. In this context, integration by parts can be utilized to demonstrate that

$$\begin{aligned} D_t^\beta f(t) &= \frac{1}{\Gamma(\lceil\beta\rceil-\beta)}\left(-\left[f^{(\lceil\beta\rceil)}(\tau)\frac{(t-\tau)^{\lceil\beta\rceil-\beta}}{\lceil\beta\rceil-\beta}\right]\Bigg|_0^t + \int_0^t f^{(\lceil\beta\rceil+1)}(\tau)\frac{(t-\tau)^{\lceil\beta\rceil-\beta}}{\lceil\beta\rceil-\beta}\,\mathrm{d}\tau\right) \\ &= \frac{t^{\lceil\beta\rceil-\beta}f^{(\lceil\beta\rceil)}(0)}{\Gamma(\lceil\beta\rceil-\beta+1)} + \frac{1}{\Gamma(\lceil\beta\rceil-\beta+1)} \times \int_0^t (t-\tau)^{\lceil\beta\rceil-\beta} f^{(\lceil\beta\rceil+1)}(\tau)\,\mathrm{d}\tau. \end{aligned} \tag{21}$$

As $\beta \to \lceil\beta\rceil$, we have

$$\begin{aligned} \lim_{\beta\to\lceil\beta\rceil} D_t^\beta f(t) &= f^{(\lceil\beta\rceil)}(0) + \int_0^t f^{(\lceil\beta\rceil+1)}(\tau)\mathrm{d}\tau \\ &= f^{(\lceil\beta\rceil)}(0) + f^{(\lceil\beta\rceil)}(t) - f^{(\lceil\beta\rceil)}(0) \\ &= f^{(\lceil\beta\rceil)}(t). \end{aligned} \tag{22}$$

In parallel to the integer-order derivative, *given certain conditions* ((Diethelm, 2010)[Lemma 3.13]), the Caputo fractional derivative possesses the semigroup property as illustrated in (Diethelm, 2010)[Lemma 3.13]:

$$D_t^\varepsilon D_t^n f = D_t^{n+\varepsilon} f. \tag{23}$$

Nonetheless, it is crucial to recognize that, in general, the Caputo fractional derivative does not exhibit the semigroup property, a characteristic inherent to integer-order derivatives, as detailed in (Diethelm, 2010)[Section 3.1]. The Caputo fractional derivative also exhibits linearity, but does not adhere to the same Leibniz and chain rules as its integer counterpart. As such properties are not utilized in our work, we refer interested readers to (Diethelm, 2010)[Theorem 3.17 and Remark 3.5.].

B.2 Comparison between Riemann–Liouville and Caputo Derivative

Another well-known fractional derivative is the Riemann–Liouville derivative, which, however, sees less use in practical applications (see Appendix B.4 for more insights). In this section, we offer a succinct introduction to the Riemann–Liouville derivative and compare it with Caputo's definition. The Riemann–Liouville fractional derivative is given as

$$\widehat{D}_t^\beta f(t) := \frac{1}{\Gamma(\lceil\beta\rceil-\beta)}\frac{\mathrm{d}^{\lceil\beta\rceil}}{\mathrm{d}t^{\lceil\beta\rceil}}\int_0^t (t-\tau)^{\lceil\beta\rceil-\beta-1} f(\tau)\mathrm{d}\tau \tag{24}$$

Here again, we make the assumption that sufficient conditions are satisfied to ensure well-definedness (refer to (Diethelm, 2010)[section 2.2] for details).

We compare the Taylor expansion for the two definitions of fractional derivatives, namely the Riemann-Liouville and Caputo derivatives, with the conventional integer-order derivative. This comparison allows us to clearly highlight the distinctions among the differential equations defined under these three different approaches.

• **Classical Integer-order Taylor Expansion:** (Diethelm, 2010)[Theorem 2.C] Assuming that f has absolutely continuous $(m-1)$-st derivative, we have that for $t \in [0, b]$,

$$f(t) = \sum_{k=0}^{m-1} \frac{t^k}{k!}\frac{\mathrm{d}^k f(0)}{\mathrm{d}t^k} + J^m \frac{\mathrm{d}^m}{\mathrm{d}t^m} f(t) \tag{25}$$

where $J^n f(t) := \frac{1}{\Gamma(n)}\int_0^t (t-\tau)^{n-1} f(\tau)\,\mathrm{d}\tau$. Note that here, k *is an integer*.

• **Riemann-Liouville Fractional Taylor Expansion:** (Diethelm, 2010)[Theorem 2.24] Let $n > 0$ and $m = \lfloor n\rfloor + 1$. Assume that f is such that $J^{m-n} f$ has absolutely continuous $(m-1)$-st derivative. Then,

$$f(t) = \frac{t^{n-m}}{\Gamma(n-m+1)} J^{m-n} f(0) + \sum_{k=1}^{m-1} \frac{t^{k+n-m}}{\Gamma(k+n-m+1)} \widehat{D}_t^{k+n-m} f(0) + J^n \widehat{D}_t^n f(t). \tag{26}$$

Note that in the case $n \in \mathbb{N}$ we have $m = n+1$ and $\Gamma(n-m+1) = \Gamma(0) = \infty$, and the first term before the sum vanishes. Hence, we recover the classical result. For general n, *the order in* $\widehat{D}_t^{k+n-m}$ *is not a integer.*

• **Caputo Fractional Taylor Expansion:** (Diethelm, 2010)[Theorem 3.8.] Assume that $n \geq 0, m = \lceil n \rceil$, and f has absolutely continuous $(m-1)$-st derivative. Then

$$f(t) = \sum_{k=0}^{m-1} \frac{t^k}{k!} D_t^k f(0) + J^n D_t^n f(t). \tag{27}$$

Note *the order in D_t^k is an integer.* If we compare (25) to (27), it becomes evident that the Caputo derivative closely resembles the classical integer-order derivative in terms of Taylor expansion. This fact influences the initial conditions for the differential equations introduced in the following section.

B.3 (Caputo) Fractional Differential Equation

In this section, we first compare the initial conditions for fractional differential equations under the Riemann-Liouville and Caputo definitions. Following this, we present the precise conditions for the existence and uniqueness of the solution to the fractional differential equation. These conditions closely align with those of ordinary differential equations, which are widely assumed by integer-order continuous GNNs such as GRAND (Chamberlain et al., 2021c), GraphCON (Rusch et al., 2022), GRAND++ (Thorpe et al., 2022), GREAD (Choi et al., 2023), and CDE (Zhao et al., 2023). In short, our FROND framework with fractional dynamics seamlessly extends these integer-order continuous GNNs.

B.3.1 Riemann-Liouville Case

Drawing from the Riemann-Liouville fractional Taylor expansion, let us assume that e is a given function with the property that there exists some function g such that $g = \widehat{D}_t^\beta e$. The solution of the Riemann-Liouville differential equation of the form

$$\widehat{D}_t^\beta f = g \tag{28}$$

is given by

$$f(t) = e(t) + \sum_{j=1}^{\lceil \beta \rceil} c_j t^{n-j} \tag{29}$$

where c_j are arbitrary constants. In other words, to uniquely determine the solution from (26), we need to know the value of $\widehat{D}_t^{k+n-m} f(0)$. This is akin to a k order ordinary differential equation where the initial conditions are assumed as $\frac{\mathrm{d}^k}{\mathrm{d}t^k} f(0)$, *with the distinction that the order in $\widehat{D}_t^{k+n-m}$ is not an integer.*

B.3.2 Caputo Case

Similarly, if e is a given function with the property that $e = D_t^\beta g$ and if we intend to solve

$$D_t^\beta f = g \tag{30}$$

then we find

$$f(t) = e(t) + \sum_{j=1}^{\lceil \beta \rceil} c_j t^{\lceil \beta \rceil - j} \tag{31}$$

once more, with c_j as arbitrary constants. Thus, to obtain a unique solution, it is natural to prescribe the values of *integer order derivatives* $f(0), D_t^1 f(0), \ldots, D_t^{\lceil \beta \rceil - 1} f(0)$ in the Caputo setting, *mirroring traditional ordinary differential equations.*

B.3.3 Existence and Uniqueness of the (Caputo) Solution

Next, we delve into a general Caputo fractional differential equation, presented as follows:

$$D_t^\beta y(t) = g(t, y(t)) \tag{32}$$

conjoined with suitable initial conditions. As hinted in (30) and (31), the initial conditions take the form:

$$D_t^k y(0) = y_0^{(k)}, \quad k = 0, 1, \ldots, \lceil \beta \rceil - 1. \tag{33}$$

The following theorem addresses the existence and uniqueness of solutions:

- **Caputo existence and uniqueness theorem:** (Diethelm, 2010)[Theorem 6.8] Let $y_0^{(0)}, \ldots, y_0^{(m-1)} \in \mathbb{R}$ and $h^* > 0$. Define the set $G := [0, h^*] \times \mathbb{R}$ and let the function

$g : G \to \mathbb{R}$ be continuous and fulfill a *Lipschitz condition* with respect to the second variable, i.e.,

$$|g(x, y_1) - g(x, y_2)| \leq L |y_1 - y_2|$$

for some constant $L > 0$ independent of x, y_1, and y_2. Then there *uniquely exists* function $y \in C[0, h^*]$ solving the initial value problem (32) and (33).

For a point of reference, we also provide the well-known Picard–Lindelöf uniqueness theorem for first-order ordinary differential equations.

- **Picard–Lindelöf theorem** (Hartman, 2002)[Page 8] Let $D \subseteq \mathbb{R} \times \mathbb{R}^n$ be a closed rectangle with $(t_0, y_0) \in \operatorname{int} D$, the interior of D. Let $g : D \to \mathbb{R}^n$ be a function that is continuous in t and *Lipschitz continuous* in y. Then, there exists some $\varepsilon > 0$ such that the initial value problem

$$y'(t) = g(t, y(t)), \quad y(t_0) = y_0.$$

has a *unique solution* $y(t)$ on the interval $[t_0, t_0 + \varepsilon]$.

This allows us to draw parallels between the existence and uniqueness theorem of the Caputo fractional differential equation and its integer-order ordinary differential equation equivalent. We also remind readers that standard neural networks, as compositions of linear maps and pointwise non-linear activation functions with bounded derivatives (such as fully-connected and convolutional networks), satisfy global Lipschitz continuity with respect to the input. For attention neural networks, which are compositions of softmax and matrix multiplication, we observe local Lipschitz continuity. To see this, suppose $\mathbf{v} = \operatorname{softmax}(\mathbf{u}) \in \mathbb{R}^{n \times 1}$. Then

$$\frac{\mathrm{d}\mathbf{v}}{\partial \mathbf{u}} = \operatorname{diag}(\mathbf{v}) - \mathbf{v}\mathbf{v}^\top = \begin{bmatrix} v_1(1 - v_1) & -v_1 v_2 & \dots & -v_1 v_n \\ -v_2 v_1 & v_2(1 - v_2) & \dots & -v_2 v_n \\ \vdots & \vdots & \ddots & \vdots \\ -v_n v_1 & -v_n v_2 & \dots & v_n(1 - v_n) \end{bmatrix}.$$

For bounded input, we have a bounded Jacobian. All the integer-order continuous GNN works, such as recent contributions like GRAND (Chamberlain et al., 2021c), GraphCON (Rusch et al., 2022), GRAND++ (Thorpe et al., 2022), GREAD (Choi et al., 2023) and CDE (Zhao et al., 2023) assume the uniqueness of the ODE solutions. *This means that all the integer-order continuous GNNs can be extended by our FROND framework with fractional dynamics.*

B.4 Reasons for Choosing Caputo Derivative

We now explain the reasons behind our preference for the Caputo fractional derivative:

1. As previously discussed, Caputo fractional differential equations align with ordinary differential equations concerning initial conditions.

2. The Caputo fractional derivative maintains a more intuitive resemblance to the integer-order derivative and satisfies the significant property of equating to zero when applied to a constant. This property is not satisfied by the Riemann-Liouville fractional derivative. Refer to (Diethelm, 2010)[Example 2.4. and Example 3.1.] for further clarification.

3. Given its widespread application in the literature for practical use cases, numerical methods for solving Caputo fractional differential equations have been meticulously developed and exhaustively analyzed (Diethelm, 2010; Diethelm et al., 2004; Deng, 2007).

We remind readers that numerous methods for training neural ODEs, and consequently updating the weights θ in the neural network have been proposed. These include the autodifferentiation technique in PyTorch (Yan et al., 2018; Paszke et al., 2017), the adjoint sensitivity method (Chen et al., 2018b), and Snode (Quaglino et al., 2019). In our work, we employ the most straightforward autodifferentiation technique for training FROND with fractional neural differential equations, leveraging the numerical solvers outlined in (Diethelm, 2010; Diethelm et al., 2004; Deng, 2007). While we plan to investigate more sophisticated techniques for training FROND in future work, we have open-sourced our current solver implementations. We believe these will serve as valuable tools for the GNN community, encouraging the advancement of a unique class of GNNs that incorporate memory effects (fractional dynamics).

C Numerical Solvers for FROND

In traditional integer-order continuous GNNs (Chamberlain et al., 2021c; Thorpe et al., 2022; Rusch et al., 2022; Song et al., 2022; Choi et al., 2023; Zhao et al., 2023), the time parameter t serves as a continuous analog to GNN layers, resembling the concept of neural ODEs (Chen et al., 2018b) as continuous residual networks. Time discretization plays a crucial role in many numerical solvers for neural ODEs. For example, the explicit Euler scheme reduces neural ODEs to residual networks with shared hidden layers (Chen et al., 2018b). More sophisticated discretization methods, such as adaptive step size solvers (Atkinson et al., 2011), provide accurate solutions but require additional computational resources.

Unlike prior studies, our work involves fractional-order differential equations, which are more complex than ODEs when the derivative order β takes non-integer values. We present the *fractional Adams–Bashforth–Moulton method* with three variants utilized in this work, demonstrating how the time parameter continues to serve as a continuous analog to the layer index and how the non-local nature of fractional derivatives leads to nontrivial dense or skip connections between layers. Additionally, we also present one implicit L1 solver for solving FROND when β is not an integer. It is worth noting that various neural ODE solvers remain applicable for FROND when β is an integer.

We first recall the FROND framework

$$D_t^\beta \mathbf{X}(t) = \mathcal{F}(\mathbf{W}, \mathbf{X}(t)), \quad \beta > 0,$$

where β denotes the fractional order of the derivative, and $\mathcal{F}$ is a dynamic operator on the graph like the models presented in Section 2.2. The initial condition is set as $\mathbf{X}^{(\lceil\beta\rceil-1)}(0) = \ldots = \mathbf{X}(0) = \mathbf{X}$ consisting of the preliminary node features, akin to the initial conditions seen in ODEs.

C.1 Basic predictor

Referencing (Diethelm et al., 2004), we first employ a preliminary numerical solver called "predictor" through time discretisation $t_j = jh$, where the discretisation parameter h is a small positive value:

$$_{\mathrm{P}}\mathbf{X}^{(k)} = \sum_{j=0}^{\lceil\beta\rceil-1} \frac{t_k^j}{j!}\mathbf{X}^{[j]}(0) + \frac{1}{\Gamma(\beta)}\sum_{j=0}^{k-1}\mu_{j,k}\mathcal{F}(\mathbf{W}, \mathbf{X}^{(j)}), \tag{34}$$

where $\mu_{j,n} = \frac{h^\beta}{\beta}\left((n-j)^\beta - (n-1-j)^\beta\right)$, k denotes the discrete time index (iteration), and $t_k = kh$ represents the discretized time steps. $\mathbf{X}^{(k)}$ is the numerical approximation of $\mathbf{X}(t_k)$. When $\beta = 1$, this method simplifies to the Euler solver in (Chen et al., 2018b; Chamberlain et al., 2021c) as $\mu_{j,n} \equiv h$, yielding $_{\mathrm{P}}\mathbf{X}^{(k)} = \mathbf{X}^{(k-1)} + h\mathcal{F}(\mathbf{W}, \mathbf{X}^{(k-1)})$. Thus, our basic predictor can be considered as the fractional Euler method or fractional Adams–Bashforth method, which is a generalization of the Euler method used in (Chen et al., 2018b; Chamberlain et al., 2021c). However, when $\beta < 1$, we need to utilize the full memory $\{\mathcal{F}(\mathbf{W}, \mathbf{X}^{(j)})\}_{j=0}^{k-1}$.

The block diagram of this basic predictor, shown in Fig. 3, reveals that our framework introduces nontrivial dense or skip connections between layers. A more refined visualization is conveyed in Fig. 4, elucidating the manner in which information propagates through layers and the graph's spatial domain.

C.2 Predictor-corrector

The corrector formula from (Diethelm et al., 2004), a fractional variant of the one-step Adams-Moulton method, refines the initial approximation using the predictor $_{\mathrm{P}}\mathbf{X}^{(k)}$ as follows:

$$\mathbf{X}^{(k)} = \sum_{j=0}^{\lceil\beta\rceil-1} \frac{t_k^j}{j!}\mathbf{X}^{[j]}(0) + \frac{1}{\Gamma(\beta)}\sum_{j=0}^{k-1}\eta_{j,n}\mathcal{F}(\mathbf{W}, \mathbf{X}^{(j)}) + \frac{1}{\Gamma(\beta)}\eta_{n,n}\mathcal{F}(\mathbf{W}, {}_{\mathrm{P}}\mathbf{X}^{(k)}). \tag{35}$$

Here we show the coefficients $\eta_{j,n}$ in the predictor-corrector variant (35) from (Diethelm et al., 2004):

$$\eta_{j,n}(\beta) = \frac{h^\beta}{\beta(\beta+1)} \times \begin{cases} (n-1)^{\beta+1} - (n-1-\beta)n^\beta & \text{if } j = 0, \\ (n-j+1)^{\beta+1} + (n-1-j)^{\beta+1} - 2(n-j)^{\beta+1} & \text{if } 1 \le j \le n-1, \\ 1 & \text{if } j = n. \end{cases} \tag{36}$$

C.3 SHORT MEMORY PRINCIPLE

When T is large, computational time complexity becomes a challenge due to the non-local nature of fractional derivatives. To mitigate this, (Deng, 2007; Podlubny, 1999) suggest leveraging the short memory principle to modify the summation in (18) and (35) to $\sum_{j=n-K}^{n-1}$. This corresponds to employing a shifting memory window with a fixed width K. The block diagram is depicted in Fig. 3.

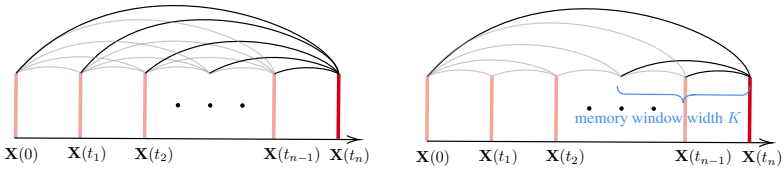

Figure 3: Diagrams of fractional Adams–Bashforth–Moulton method with full (left) and short (right) memory.

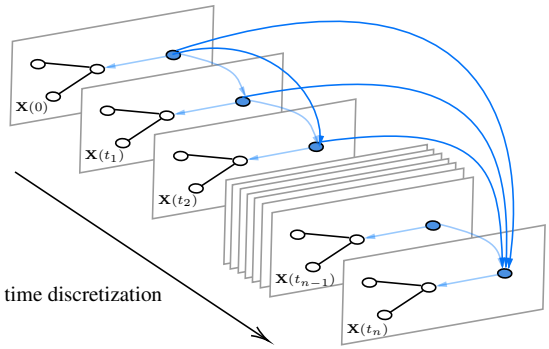

Figure 4: Model discretization in FROND with the basic predictor solver. Unlike the Euler discretization in ODEs, FDEs incorporate connections to historical times, introducing memory effects. Specifically, the dark blue connections observed in FDEs are absent in ODEs. The weight of these skip connections correlates with $\eta_{j,n}(\beta)$ as detailed in (36).

C.4 L1 SOLVER

The L1 scheme is one of the most popular methods to approximate the Caputo fractional derivative in time. It utilizes a backward differencing method for effective approximation of derivatives. Referencing (Gao & Sun, 2011; Sun & Wu, 2006), we have the L1 approximation of Caputo fractional derivative as follows:

$$D_t^\beta \mathbf{X}^{(k)} \approx \mu \sum_{j=0}^{k-1} R_{k,j}^\beta (\mathbf{X}^{(j+1)} - \mathbf{X}^{(j)})$$

where h is the temporal step size,

$$\mu = \frac{1}{h^\beta \Gamma(2-\beta)}, \qquad R_{k,j}^\beta = (k-j)^{1-\beta} - (k-j-1)^{1-\beta}, \qquad 0 \le j \le k-1.$$

Applying the L1 solver for our problem, we obtain

$$\mu \sum_{j=0}^{k-1} R_{k,j}^\beta (\mathbf{X}^{(j+1)} - \mathbf{X}^{(j)}) = (\mathbf{A}(\mathbf{X}^{(k)}) - \mathbf{I})\mathbf{X}^{(k)}.$$

Manipulating the above equation, we have

$$\mathbf{X}^{(k)} - \frac{1}{\mu}(\mathbf{A}(\mathbf{X}^{(k)}) - \mathbf{I})\mathbf{X}^{(k)}) = \mathbf{X}^{(k-1)} - \sum_{j=0}^{k-2} R_{k,j}^\beta (\mathbf{X}^{(j+1)} - \mathbf{X}^{(j)})$$

The above formula is an implicit nonlinear scheme. To solve it without calculating the inversion of a matrix, we propose the following iteration method:

(1) Compute a basic approximation of $\mathbf{X}(t_k)$ with the following formula:

$$_{\mathrm{P}}\mathbf{X}^{(k)} - \frac{1}{\mu}(\mathbf{A}(\mathbf{X}^{(k-1)}) - \mathbf{I})\mathbf{X}^{(k-1)} = \mathbf{X}^{(k-1)} - \sum_{j=0}^{k-2} R_{k,j}^{\beta}(\mathbf{X}^{(j+1)} - \mathbf{X}^{(j)}).$$

(2) Substitute the above $_{\mathrm{P}}\mathbf{X}^{(k)}$ into the implicit scheme to update $\mathbf{X}^{(k)}$:

$$\mathbf{X}^{(k)} - \frac{1}{\mu}(\mathbf{A}(_{\mathrm{P}}\mathbf{X}^{(k)}) - \mathbf{I})_{\mathrm{P}}\mathbf{X}^{(k)} = \mathbf{X}^{(k-1)} - \sum_{j=0}^{k-2} R_{k,j}^{\beta}(\mathbf{X}^{(j+1)} - \mathbf{X}^{(j)}). \tag{37}$$

The step (2) can be repeated multiple times to obtain an accurate approximation of $\mathbf{X}(t_k)$.

D Datasets, Settings and More Experiments for **F-GRAND** model

D.1 Datasets

The dataset statistics used in Table 1 are provided in Table 5. Following the experimental framework in (Chamberlain et al., 2021c), we select the largest connected component from each dataset, except for the tree-like graph datasets (Airport and Disease). However, for the study of over-smoothness, we use a fixed data splitting approach over the entire datasets, as described in (Chami et al., 2019).

Table 5: Dataset Statistics used in Table 1

Dataset	Type	Classes	Features	Nodes	Edges
Cora	citation	7	1433	2485	5069
Citeseer	citation	6	3703	2120	3679
PubMed	citation	3	500	19717	44324
Coauthor CS	co-author	15	6805	18333	81894
Computers	co-purchase	10	767	13381	245778
Photos	co-purchase	8	745	7487	119043
CoauthorPhy	co-author	5	8415	34493	247962
OGB-Arxiv	citation	40	128	169343	1166243
Airport	tree-like	4	4	3188	3188
Disease	tree-like	2	1000	1044	1043

Table 6: Dataset and graph statistics used in Table 2

Dataset	Graphs (Fake)	Total Nodes	Total Edges	Avg. Nodes per Graph
Politifact (POL)	314 (157)	41,054	40,740	131
Gossipcop (GOS)	5464 (2732)	314,262	308,798	58

D.2 Graph Classification Details

We use the Fake-NewsNet datasets from (Dou et al., 2021), constructed based on fact-checking information obtained from Politifact and Gossipcop. The dataset incorporates four distinct node feature categories, including 768-dimensional BERT features and 300-dimensional spaCy features, which are derived using pre-trained BERT and spaCy word2vec models, respectively. Additionally, a 10-dimensional profile feature is extracted from individual Twitter accounts' profiles. Each graph within the dataset is characterized by a hierarchical tree structure, with the root node representing the news item and the leaf nodes representing Twitter users who have retweeted said news. An edge exists between a user node and the news node if the user retweeted the original news tweet, while an edge between two user nodes is established when one user retweets the news tweet from another user. This hierarchical organization facilitates the analysis of the spread and influence of both genuine and fabricated news within the Twitter ecosystem. The datasets statistics are summarized in Table 6.

D.3 IMPLEMENTATION DETAILS

Our FROND framework adheres to the experimental settings of the foundational integer-order continuous GNNs, diverging only in the introduction of fractional derivatives in place of integer derivatives. In implementing GRAND, we employ one fully-connected (FC) layer on the raw input features to obtain the initial node representations, $\mathbf{X}(0)$, for the FDE. Subsequently, we utilize another FC layer as the decoder function to process the FDE output, $\mathbf{X}(T)$, for executing downstream tasks. For more detailed information regarding the hyperparameter settings, we kindly direct the readers to the accompanying supplementary material, which includes the provided code for reproducibility. Our experiments were conducted using NVIDIA RTX A5000 graphics cards.

D.4 LARGE SCALE OGBN-PRODUCTS DATASET

In this section, we extend our evaluation to include another large-scale dataset, Ogbn-products, adhering to the experimental settings outlined in (Hu et al., 2021). For effective handling of this large dataset, we employ a mini-batch training approach, which involves sampling nodes and constructing subgraphs, as proposed by GraphSAINT (Zeng et al., 2020). Upon examination, we observe that F-GRAND-l demonstrates superior performance compared to both GRAND-l and the GCN model, although it falls slightly short of the performance exhibited by GraphSAGE. This outcome could potentially be attributed to the insufficient dynamic setting in (9). As such, the more advanced dynamic $\mathcal{F}(\mathbf{W}, \mathbf{X}(t))$ in (6) may require additional refinement.

Table 7: Node classification accuracy(%) on Ogbn-products dataset

Model	MLP	Node2vec	Full-batch GCN	GraphSAGE	GRAND-l	F-GRAND-l
Acc	61.06±0.08	72.49±0.10	75.64±0.21	78.29±0.16	75.56±0.67	77.25±0.62

D.5 PERFORMANCE OF DIFFERENT SOLVER VARIANTS

In this work, we introduce two types of solvers with distinct variants. We evaluate the performance of these variants in Table 8. Specifically, we run F-GRAND on the Cora and Airport datasets with $h = 1$ and $T = 64$. The solver variants perform comparably. For the Cora dataset, the fractional Adams–Bashforth–Moulton method with a short memory parameter of $K = 10$ performs slightly worse than the other variants. However, it demonstrates comparable performance to other solver variants on the Airport dataset.

Table 8: Node classification accuracy(%) under different solver when time $T = 64$

	Predictor(18)	Predictor-Corrector (35)	Short Memory	Implicit L1
Cora($\beta = 0.6$)	83.44±0.91	83.45±1.09	81.51±1.07	82.85±1.08
Airport($\beta = 0.1$)	97.41±0.42	96.85±0.36	97.23±0.59	96.06±1.59

Table 9: Node classification accuracy based on memory K on the Cora dataset when time $T = 40$.

memory K	1	5	10	15	20	25	30	35	40
Accuracy (%)	74.9±0.8	80.8±0.8	83.3±1.1	83.9±1.2	84.2±1.1	84.1±1.2	84.5±1.1	84.1±1.1	84.8±1.1
Inference (ms)	9.81	17.53	24.97	32.03	38.79	42.99	45.27	48.70	48.35

D.5.1 FURTHER CLARIFICATION ON TWO ACCURACIES

This section aims to clarify potential ambiguities surrounding the term "accuracy" by distinguishing between "task accuracy" and "numerical accuracy." Task accuracy pertains to the performance of GNNs on tasks such as node classification. In contrast, numerical accuracy relates to the precision of numerical solutions to FDEs, a critical concern in mathematics.

For example, generally, a larger K value in the Short Memory solver might enhance both numerical and GNN task accuracy. However, it comes with the trade-off of demanding more computational

resources. Furthermore, the two accuracies are related, but not equivalent to each other. For added clarity, we conducted an ablation study on the Cora dataset, keeping all parameters constant except for the memory parameter K. The outcomes of this study are detailed in Table 9. Our observations indicate that while increasing the value of K can improve numerical accuracy and potentially GNN task accuracy, the computational cost also rises. Notably, the gains in task accuracy plateau beyond a K value of 15.

We also remind the readers that in the literature, to solve FDEs, there exist other more numerically accurate solvers like (Jin et al., 2017; Tian et al., 2015; Lv & Xu, 2016) that use higher convergence order. In general, these kinds of solvers can theoretically reduce computation cost and memory storage, as we can obtain the same numerical accuracy using larger step sizes compared to lower-order solvers. It does not aim to improve GNN task accuracy as we can take smaller step sizes to achieve this, but it may be helpful for other performances like computation cost and memory storage reduction. In our paper, we focus on task accuracy. Therefore, classical solvers are used in our work. Nonetheless, more numerically accurate solvers could potentially benefit other applications of fractional dynamics, particularly when GNNs are utilized to simulate and forecast real physical systems.

D.6 Computation Time

It should be emphasized that our FROND framework *does not introduce any additional training parameters* to the backbone integer-order continuous GNNs. Instead, we simply modify the integration method from standard integration to fractional integration.

In this section, we report the inference time of the different solver variants in Tables 10 to 13. For comparison, we consider the neural ODE solver for $\beta = 1$, which includes Euler, RK4, Implicit Adams, and dopri5 methods as per in the paper (Chen et al., 2018b). We observe that when $T = 4$, the inference time required by the FROND solver variants is similar to that of the ODE Euler solver. However, for larger $T = 64$, the basic Predictor (18) solver requires more inference time than Euler and is comparable to RK4. For more accurate approximation solver variants (35) and (37) incorporating the corrector formula, Tables 12 and 13 show that these methods require more computational time as the number of iterations increases. While the advantages of these solvers might not be pronounced for GNN node classification tasks, they could provide benefits for other applications of fractional dynamics, such as when GNNs are used to simulate and forecast real physical systems.

Table 10: Average time under different solvers when time $T = 4$ and hidden dimension is 64 on Cora dataset

	Predictor(18)	Predictor-Corrector(35)	Short Memory	Implicit L1	Euler	RK4	Implicit Adams	dopri5
Inference time (ms)	0.98	1.67	0.98	0.62	0.96	2.06	3.20	11.91

Table 11: Average time under different solvers when time $T = 64$ and hidden dimension is 64 on Cora dataset

	Predictor(18)	Predictor-Corrector(35)	Short Memory	Implicit L1	Euler	RK4	Implicit Adams	dopri5
Inference time (ms)	44.46	160.92	30.26	221.74	12.16	42.66	103.46	66.15

Table 12: Average time of (35) and (37) with correctors, used to refine the approximation, when time $T = 4$ and hidden dimension is 64 on the Cora dataset.

Predictor-Corrector (35)	1	3	5	10
Inference time (ms)	1.67	3.31	4.74	8.34

Implicit-L1 (37)	1	3	5	10
Inference time (ms)	0.62	1.04	1.48	2.55

Table 13: Average time of (35) and (37) with correctors, used to refine the approximation, when time $T = 64$ and hidden dimension is 64 on the Cora dataset.

Predictor-Corrector (35)	1	3
Inference time (ms)	160.92	442.88
Implicit-L1 (37)	1	3
Inference time (ms)	221.74	441.60

D.7 Continued Study of over-smoothness

D.7.1 Node Classification accuracy

To corroborate that FROND mitigates the issue of oversmoothing and performs well with an increasing number of layers, we conducted an experiment employing the basic predictor with up to 128 layers in the main paper. The results are presented in Fig. 2. For this experiment, we utilized the fixed data splitting approach for the Cora and Citeseer dataset without using the Largest Connected Component (LCC) as described in (Chami et al., 2019).

In the supplementary material, we further probe oversmoothing by conducting experiments with an increased number of layers, reaching up to 256. The results of these experiments are illustrated in Table 14. From our observations, F-GRAND-l maintains a consistent performance level even as the number of layers escalates. This contrasts with GRAND-l, where there is a notable performance decrease with the increase in layers. For instance, on the Cora datasets, the accuracy of GRAND-l drops from 81.29% with 4 layers to 73.37% with 256 layers. In stark contrast, our F-GRAND-l model exhibits minimal performance decrease on this dataset. On the Airport dataset, F-GRAND-l registers a slight decrease to 94.91% with 256 layers from 97.0% with 4 layers. However, the performance of GRAND-l significantly drops to 53.0%. These observations align with our expectations, as Theorem 2 predicts a slow algebraic convergence rate, while GRAND exhibits a more rapid performance degradation.

Additionally, we note that the optimal number of layers for F-GRAND is 64 on the Cora and Airport datasets, whereas on the Cirtesser dataset, the best performance is achieved with 16 layers.

Table 14: oversmoothing mitigation under fixed data splitting without LCC

Dataset	Model	4	8	16	32	64	80	128	256
Cora	GCN	81.35±1.27	15.3±3.63	19.70±7.06	21.86±6.09	13.0±0.0	13.0±0.0	13.0±0.0	13.0±0.0
	GAT	80.95±2.28	31.90±0.0	31.90±0.0	31.90±0.0	31.90±0.0	31.90±0.0	31.90±0.0	31.90±0.0
	GRAND-l	81.29±0.43	82.95±0.52	82.48±0.46	81.72±0.35	81.33±0.22	81.07±0.44	80.09±0.43	73.37±0.59
	F-GRAND-l	81.17±0.75	82.68±0.64	83.05±0.81	82.90±0.81	83.44±0.91	82.85±0.89	82.34±0.83	81.74±0.53
Citeseer	GCN	68.84±2.46	61.58±2.09	10.64±1.79	7.7±0.0	7.7±0.0	7.7±0.0	7.7±0.0	7.7±0.0
	GAT	65.20±0.57	18.10±0.0	18.10±0.0	18.10±0.0	18.10±0.0	18.10±0.0	18.10±0.0	18.10±0.0
	GRAND-l	70.68±1.23	70.39±0.68	70.18±0.56	68.90±1.50	68.01±1.47	67.44±1.25	63.45±2.86	56.98±1.26
	F-GRAND-l	70.68±1.23	71.04±0.68	71.08±1.12	70.83±0.90	70.27±0.86	70.50±0.76	70.32±1.67	71.0±0.45
Airport	GCN	84.77±1.45	74.43±8.19	62.56±2.16	15.27±0.0	15.27±0.0	15.27±0.0	15.27±0.0	15.27±0.0
	GAT	83.59±1.51	67.02±4.70	46.56±0.0	46.56±0.0	46.56±0.0	46.56±0.0	46.56±0.0	46.56±0.0
	GRAND-l	80.53±9.59	79.88±9.67	76.24±3.80	68.67±4.02	62.28±10.83	50.38±2.98	57.96±11.63	53.0±14.85
	F-GRAND-l	97.0±0.79	97.09±0.87	96.97±0.84	96.50±0.60	97.41±0.42	96.53±0.74	97.03±0.55	94.91±3.72

D.7.2 Dirichlet Energy

The Dirichlet Energy defined on the graph is represented as:

$$\mathbf{E}(\mathbf{X}(t)) := \sum_{i\in\mathcal{V}} \sum_{j\in\mathcal{V}} \|\mathbf{x}_i(t) - \mathbf{x}_j(t)\|_2^2 \tag{38}$$

Dirichlet Energy provides quantitative insights into the variability of features across nodes and their neighbors. Higher Dirichlet Energy implies greater diversity in node features, suggesting lower oversmoothing levels, while lower energy points to the contrary, indicating a possible risk of information loss through excessive smoothing.

Table 15: Node classification accuracy(%) under different value of β when time $T = 8$.

β	0.1	0.2	0.3	0.4	0.5	0.6	0.7	0.8	0.9	1.0
Cora	74.80±0.42	76.10±0.34	77.0±0.98	77.80±0.75	79.60±0.91	80.79±0.58	81.56±0.30	82.44±0.51	82.68±0.64	82.37±0.59
Airport	97.09±0.87	96.67±0.91	95.80±2.03	94.04±3.62	91.66±6.34	89.24±7.87	84.36±8.04	79.29±6.01	78.73±6.33	78.88±9.67

We visualize the Dirichlet Energy of both Cora and Airport datasets across different models in Figures Fig. 5 and Fig. 6, respectively. The term "number of layers" for both the GRAND and F-GRAND models refers to the time T of integration, calculated using the Euler solver and the basic predictor solver, respectively. This interpretation of layers is pivotal as it extends the discrete layer concept in traditional models to a continuous-time framework. Observations indicate that our F-GRAND model exhibits slower convergence compared to GRAND on the Cora dataset, while maintaining nearly consistent Dirichlet Energy values on the Airport dataset up to 120 layers. This consistency underscores its competence in mitigating the oversmoothing problem. As we have proven in Corollary 1, the Dirichlet Energy will *asymptotically* approach 0 at a slow algebraic rate. The sustained plot on the Airport dataset could arise from inadequacies in the layer count and the numerical precision of the solvers. Nonetheless, the depiction of Dirichlet Energy provides substantial evidence of FROND's potential in alleviating over-smoothness. It is worth highlighting that, particularly on tree-structured datasets, F-GRAND stands out as the sole model capable of alleviating over-smoothness. This observation is consistent with the findings presented in Fig. 2 of the main paper.

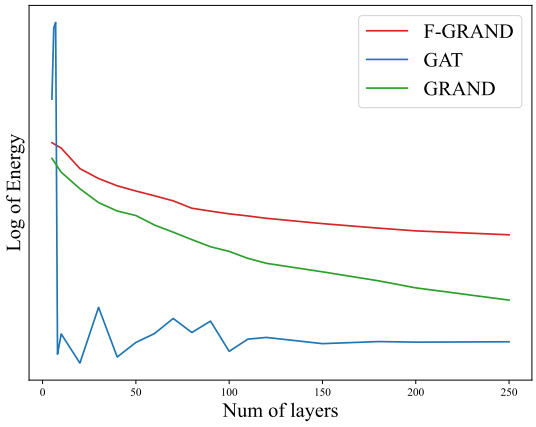

Figure 5: Dirichlet Energy of Cora dataset

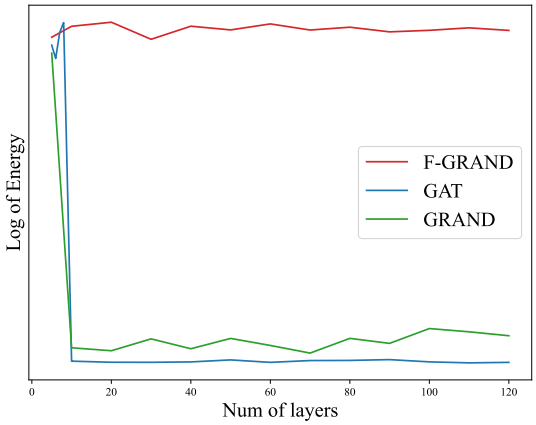

Figure 6: Dirichlet Energy of Airport dataset.

D.8 Ablation Study: Selection of β Continued

In the main paper, we explore the impact of the fractional order parameter β across a variety of graph datasets, with the results of these investigations presented in Table 3. More comprehensive details concerning the variations in β can be found in Table 15.

D.9 Robustness Against Adversarial Attacks

Despite the significant advancements GNNs have made in inference tasks on graph-structured data, they are recognized as being susceptible to adversarial attacks (Zügner et al., 2018). Adversaries, aiming to deceive a trained GNN, can either introduce new nodes into the graph during the inference phase, known as an injection attack (Wang et al., 2020; Zheng et al., 2022; Zou et al., 2021; Hussain et al., 2022), or manipulate the graph's topology by adding or removing edges, termed as a modification attack (Chen et al., 2018a; Waniek et al., 2018; Du et al., 2017). In this section, we present preliminary experiments assessing the robustness of our model against adversarial attacks. Specifically, we carry out graph modification adversarial attacks using the Metattack method (Zügner & Günnemann, 2019). Our approach adheres to the attack setting described in Pro-GNN (Jin et al., 2020), and we utilize the perturbed graph provided by the DeepRobust library (Li et al., 2020b)

to ensure a fair comparison. The perturbation rate, indicating the proportion of altered edges, is incrementally adjusted in 5% steps from 0% to 25%.

The results of these experiments are presented in Table 16. It should be noted that the impact of Meta-attacks with higher strengths detrimentally affects the performance of all models under test. However, our FROND-nl model consistently demonstrates enhanced resilience against adversarial attacks compared to the baselines, including GRAND-nl. For instance, at a perturbation rate of 25%, F-GRAND-nl outshines the baselines by an estimated margin of 10 to 15% on the Cora dataset.

Comprehensive testing against a variety of adversarial attack methods constitutes an important direction for our future work.

Table 16: Node classification accuracy (%) under **modification, poisoning, non-targeted** attack (Metattack) in **transductive** learning.

Dataset	Ptb Rate(%)	GGN	GAT	GRAND-nl	F-GRAND-nl
Cora	0	83.50±0.44	83.97±0.65	83.14±1.06	83.48±1.08
	5	76.55±0.79	80.44±0.74	80.54±1.17	80.25±0.90
	10	70.39±1.28	75.61±0.59	76.59±1.21	77.94±0.48
	15	65.10±0.71	69.78±1.28	71.62±1.39	75.14±1.16
	20	59.56±2.72	59.94±0.92	57.52±1.20	69.04±1.13
	25	47.53±1.96	54.78±0.74	53.70±1.91	63.40±1.44
Citeseer	0	71.96±0.55	73.26±0.83	71.40±1.08	70.14±0.83
	5	70.88±0.62	72.89±0.83	70.99±1.12	70.0±1.72
	10	67.55±0.89	70.63±0.48	68.83±1.31	68.64±1.11
	15	64.52±1.11	69.02±1.09	66.78±0.92	67.90±0.41
	20	62.03±3.49	61.04±1.52	58.95±1.33	65.84±0.75
	25	56.94±2.09	61.85±1.12	60.52±1.29	66.50±1.16

D.10 Comparison between Riemann-Liouville (RL) derivative and Caputo Derivative

The underlying rationale for opting for the Caputo derivative over the Riemann-Liouville (RL) derivative is extensively delineated in Appendix B.4. However, a supplementary experiment was conducted utilizing the RL derivative in lieu of the Caputo derivative, the results of which are documented in Table 17. It can be observed that the task accuracies for both approaches are very similar. Further investigations on the use of different fractional derivatives and how to optimize the whole model architecture to adapt to a particular choice will be explored in future work.

Table 17: Comparison between RL-GRAND-l (using Riemann-Liouville derivative) and the original F-GRAND-l (using Caputo derivative).

Method	Cora	Citeseer	Pubmed	CoauthorCS	Computer	Photo	CoauthorPhy	Airport	Disease
GRAND-l	83.6±1.0	73.4±0.5	78.8±1.7	92.9±0.4	83.7±1.2	92.3±0.9	93.5±0.9	80.5±9.6	74.5±3.4
RL-GRAND-l	84.6±1.2	74.2±1.0	80.1±1.2	92.8±0.3	87.4±1.1	93.3±0.7	94.1±0.3	96.2±0.2	90.7±1.3
F-GRAND-l	84.8±1.1	74.0±1.5	79.4±1.5	93.0±0.3	84.4±1.5	92.8±0.6	94.5±0.4	98.1±0.2	92.4±3.9

D.11 Tree-like Data Fractal Dimension

Table 18: Comparison between the estimated fractal dimension, the best order β and the δ-hyperbolicity

Dataset	Disease	Airport	Pubmed	Citeseer	Cora
fractal dimension	2.47	2.17	2.25	0.62	1.22
best β (F-GRAND-l)	0.6	0.5	0.9	0.9	0.9
best β (F-GRAND-nl)	0.7	0.1	0.4	0.9	0.9
δ-hyperbolicity	0.0	1.0	3.5	4.5	11.0

In Fig. 7, using the Compact-Box-Burning algorithm from (Song et al., 2007), we compute the fractal dimension for some datasets that have moderate sizes. As noted in Table 1, there is a clear trend

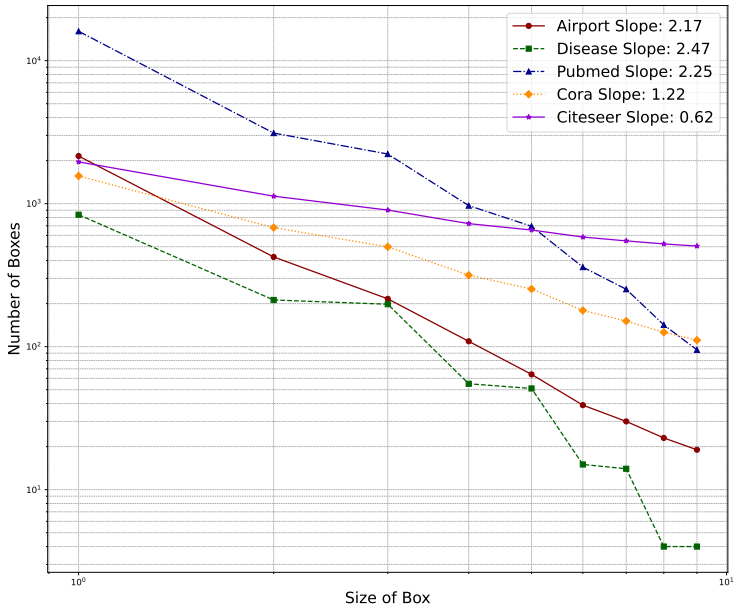

Figure 7: The fractal dim of datasets. We use the Compact-Box-Burning algorithm in (Song et al., 2007) to compute the log-log slope (fractal dim) of the box size and the minimum number of boxes needed to cover the graph.

between δ-hyperbolicity (as referenced in (Chami et al., 2019) for assessing tree-like structures—with lower values suggesting more tree-like graphs) and the fractal dimension of datasets. Specifically, a lower δ-hyperbolicity corresponds to a larger fractal dimension. As discussed in Sections 1 and 4, we believe that our fractional derivative D_t^β effectively captures the fractal geometry in the datasets. Notably, we discerned a trend: a larger fractal dimension typically corresponds to a smaller optimal β.

E More Dynamics in FROND Framework

E.1 Review of Graph ODE Models

GRAND++: The work by (Thorpe et al., 2022) introduces graph neural diffusion with a source term, aimed at graph learning in scenarios with a limited quantity of labeled nodes. This approach leverages a subset of feature vectors, those associated with labeled nodes, indexed by $\mathcal{I}$, and considered "trustworthy" to act as a source term. It adheres to (4) and (5), incorporating an additional source term, facilitating the propagation of information from nodes in $\mathcal{I}$ to node i.

$$\frac{\mathrm{d}\mathbf{X}(t)}{\mathrm{d}t} = F(\mathbf{X}(t)) + s(\{\mathbf{x}_i\}_{i\in\mathcal{I}}) \tag{39}$$

Here, $\mathcal{I}$ denotes the set of source nodes, $s(\cdot)$ represents a source function, and $F(\cdot)$ embodies the function depicting the right-hand side of (4) and (5). The model is manifested in two variations, respectively denoted as GRAND++-nl and GRAND++-l.

GraphCON: Inspired by oscillator dynamical systems, GraphCON (Rusch et al., 2022) is defined through the employment of second-order ODEs. It is crucial to highlight that, for computational efficiency, the second-order ODE is decomposed into two first-order ODEs:

$$\frac{\mathrm{d}\mathbf{Y}(t)}{\mathrm{d}t} = \sigma(\mathbf{F}_\theta(\mathbf{X}(t), t)) - \gamma\mathbf{X}(t) - \tilde{\alpha}\mathbf{Y}(t), \qquad \frac{\mathrm{d}\mathbf{X}(t)}{\mathrm{d}t} = \mathbf{Y}(t), \tag{40}$$

where $\sigma(\cdot)$ is the activation function, $\mathbf{F}_\theta(\mathbf{X}(t), t)$ is the neural network function with parameters θ, γ and $\tilde{\alpha}$ are learnable coefficients, and $\mathbf{Y}(t)$ is the velocity term converting the second-order ODE to two first-order ODEs.

Analogous to the GRAND model, the GraphCON model is also available in both linear (GraphCON-l)

and non-linear (GraphCON-nl) versions concerning time. The differentiation between these versions is determined by whether the function $\mathbf{F}_\theta$ undergoes updates based on time t.

CDE: With the objective of addressing heterophilic graphs, the paper (Zhao et al., 2023) integrates the concept of convection-diffusion equations (CDE) into GNNs, leading to the proposition of the neural CDE model: This innovative model incorporates a convection term and introduces a unique velocity for each node, aiming to preserve diversity in heterophilic graphs. The corresponding formula is illustrated in (41).

$$\frac{\mathrm{d}\mathbf{X}(t)}{\mathrm{d}t} = (\mathbf{A}(\mathbf{X}(t)) - \mathbf{I})\mathbf{X}(t) + \mathrm{div}(\mathbf{V}(t) \circ \mathbf{X}(t)) \tag{41}$$

In this equation, $\mathbf{V}(t)$ represents the velocity field of the graph at time t, $\mathrm{div}(\cdot)$ denotes the divergence operator as defined in the paper (Chamberlain et al., 2021c; Song et al., 2022), and $\circ$ symbolizes the element-wise (Hadamard) product.

GREAD: To address the challenges posed by heterophilic graphs, the authors in (Choi et al., 2023) present the GREAD model. This model enhances the GRAND model by incorporating a reaction term, thereby formulating a diffusion-reaction equation within GNNs. The respective formula is depicted in (42), and the paper offers various alternatives for the reaction term.

$$\frac{\mathrm{d}\mathbf{X}(t)}{\mathrm{d}t} = -\alpha\mathbf{L}(\mathbf{X}(t)) + \alpha r(\mathbf{X}(t)) \tag{42}$$

In this equation, $r(\mathbf{X}(t))$ represents the reaction term, and α is a trainable parameter used to balance the impact of each term.

E.2 F-GRAND++

Building upon the GRAND++ model (Thorpe et al., 2022), we define F-GRAND++ as follows:

$$D_t^\beta \mathbf{X}(t) = F(\mathbf{X}(t)) + s(\{\mathbf{x}_i\}_{i\in\mathcal{I}}) \tag{43}$$

We follow the same experimental settings as delineated in the GRAND++ paper. Given that the primary focus of GRAND++ is the model's performance under limited-label scenarios, our experiments also align with this setting. The sole distinction lies in the incorporation of fractional dynamics. Within this framework, we substitute the ordinary differential equation $\frac{\mathrm{d}\mathbf{X}(t)}{\mathrm{d}t}$ used in GRAND++ with our FROND fractional derivative $D_t^\beta \mathbf{X}(t)$. The optimal β is determined through hyperparameter tuning. When $\beta = 1$, F-GRAND++ seamlessly reverts to GRAND++, and the results from the original paper are reported. Our observations distinctly indicate that the Fractional-GRAND++ consistently surpasses the performance of the original GRAND++ in nearly all scenarios. We also present the complete comparison results in Table 20, where it is evident that F-GRAND++ demonstrates greater effectiveness in learning with low labeling rates compared to GRAND++, GRAND, and other baseline methods.

Table 19: Node classification results (%) under limited-label scenarios

Model	pre class	Cora	Citeseer	Pubmed	CoauthorCS	Computer	Photo
GRAND++	1	54.94±16.09	58.95±9.59	65.94±4.87	60.30±1.50	67.65±0.37	83.12±0.78
F-GRAND++	1	**57.31±8.89**	**59.11±6.73**	**65.98±2.72**	**67.71±1.91**	67.65±0.37	83.12±0.78
	β	0.95	0.95	0.85	0.7	1.0	1.0
GRAND++	2	66.92±10.04	64.98±8.31	69.31±4.87	76.53±1.85	74.47±1.48	83.71±0.90
F-GRAND++	2	**70.09±8.36**	64.98±8.31	**69.37±5.36**	**77.97±2.35**	**78.85±0.96**	83.71±0.90
	β	0.9	1.0	0.95	0.5	0.8	1.0
GRAND++	5	77.80±4.46	70.03±3.63	71.99±1.91	84.83±0.84	82.64±0.56	88.33±1.21
F-GRAND++	5	**78.79±1.66**	**70.26±2.36**	**73.38±5.67**	**86.09±2.09**	82.64±0.56	**88.56±0.67**
	β	0.9	0.8	0.9	0.8	1.0	0.75
GRAND++	10	80.86±2.99	72.34±2.42	75.13±3.88	86.94±0.46	82.99±0.81	90.65±1.19
F-GRAND++	10	**82.73±0.81**	**73.52±1.44**	**77.15±2.87**	**87.85±1.44**	**83.26±0.41**	**91.15±0.52**
	β	0.95	0.9	0.95	0.6	0.7	0.95
GRAND++	20	82.95±1.37	73.53±3.31	79.16±1.37	90.80±0.34	85.73±0.50	93.55±0.38
F-GRAND++	20	**84.57±1.07**	**74.81±1.78**	**79.96±1.68**	**91.03±0.72**	**85.78±0.43**	93.55±0.38
	β	0.9	0.85	0.95	0.9	0.9	1.0

Table 20: Full table: Classification accuracy of different GNNs trained with different number of labeled data per class (#per class) on six benchmark graph node classification tasks. The highest accuracy is highlighted in bold for each number of labeled data per class. These results show that F-GRAND++ is more effective in learning with low-labeling rates than GRAND++ and GRAND. Where available, baseline results are cited from (Thorpe et al., 2022).

Model	#per class	CORA	CiteSeer	PubMed	CoauthorCS	Computer	Photo
F-GRAND++	1	**57.31 ± 8.89**	**59.11 ± 6.73**	**65.98 ± 2.72**	**67.71 ± 1.91**	**67.65 ± 0.37**	**83.12 ± 0.78**
	2	**70.09 ± 8.36**	**64.98 ± 8.31**	**69.37 ± 5.36**	77.97 ± 2.35	**78.85 ± 0.96**	**83.71 ± 0.90**
	5	**78.79 ± 1.66**	**70.26 ± 2.36**	73.38 ± 5.67	86.09 ± 2.09	**82.64 ± 0.56**	88.56 ± 0.67
	10	**82.73 ± 0.81**	**73.52 ± 1.44**	**77.15 ± 2.87**	87.85 ± 1.44	**83.26 ± 0.41**	**91.15 ± 0.52**
	20	**84.57 ± 1.07**	**74.81 ± 1.78**	**79.96 ± 1.68**	91.03 ± 0.72	**85.78 ± 0.43**	**93.55 ± 0.38**
GRAND++	1	54.94 ± 16.09	58.95 ± 9.59	65.94 ± 4.87	60.30 ± 1.50	**67.65 ± 0.37**	**83.12 ± 0.78**
	2	66.92 ± 10.04	**64.98 ± 8.31**	69.31 ± 4.87	76.53 ± 1.85	76.47 ± 1.48	**83.71 ± 0.90**
	5	77.80 ± 4.46	70.03 ± 3.63	71.99 ± 1.91	84.83 ± 0.84	82.64 ± 0.56	88.33 ± 1.21
	10	80.86 ± 2.99	72.34 ± 2.42	75.13 ± 3.88	86.94 ± 0.46	82.99 ± 0.81	90.65 ± 1.19
	20	82.95 ± 1.37	73.53 ± 3.31	79.16 ± 1.37	90.80 ± 0.34	85.73 ± 0.50	**93.55 ± 0.38**
GRAND	1	52.53 ± 16.40	50.06 ± 17.98	62.11 ± 10.58	59.15 ± 5.73	48.67 ± 1.66	81.25 ± 2.50
	2	64.82 ± 11.16	59.55 ± 10.89	69.00 ± 7.55	73.83 ± 5.58	74.77 ± 1.85	82.13 ± 3.27
	5	76.07 ± 5.08	68.37 ± 5.00	**73.98 ± 5.08**	85.29 ± 2.19	80.72 ± 1.09	88.27 ± 1.94
	10	80.25 ± 3.40	71.90 ± 7.66	76.33 ± 3.41	87.81 ± 1.36	82.42 ± 1.10	90.98 ± 0.93
	20	82.86 ± 2.39	73.02 ± 5.89	78.76 ± 1.69	91.03 ± 0.47	84.54 ± 0.90	93.53 ± 0.47
GCN	1	47.72 ± 15.33	48.94 ± 10.24	58.61 ± 12.83	65.22 ± 2.25	49.46 ± 1.65	82.94 ± 2.17
	2	60.85 ± 14.01	58.06 ± 9.76	60.45 ± 16.20	**83.61 ± 1.49**	76.90 ± 1.49	83.61 ± 0.71
	5	73.86 ± 7.97	67.24 ± 4.19	68.69 ± 7.93	86.66 ± 0.43	82.47 ± 0.97	**88.86 ± 1.56**
	10	78.82 ± 5.38	72.18 ± 3.47	72.59 ± 3.19	88.60 ± 0.50	82.53 ± 0.74	90.41 ± 0.35
	20	82.07 ± 2.03	74.21 ± 2.90	76.89 ± 3.27	91.09 ± 0.35	82.94 ± 1.54	91.95 ± 0.11
GAT	1	47.86 ± 15.38	50.31 ± 14.27	58.84 ± 12.81	51.13 ± 5.24	37.14 ± 7.81	73.58 ± 8.15
	2	58.30 ± 13.55	55.55 ± 9.19	60.24 ± 14.44	63.12 ± 6.09	65.07 ± 8.86	76.89 ± 4.89
	5	71.04 ± 5.74	67.37 ± 5.08	68.54 ± 5.75	71.65 ± 4.53	71.43 ± 7.34	83.01 ± 3.64
	10	76.31 ± 4.87	71.35 ± 4.92	72.44 ± 3.50	74.71 ± 3.35	76.04 ± 0.35	87.42 ± 2.38
	20	79.92 ± 2.28	73.22 ± 2.90	75.55 ± 4.11	79.95 ± 2.88	80.05 ± 1.81	89.38 ± 2.48
GraphSage	1	43.04 ± 14.01	48.81 ± 11.45	55.53 ± 12.71	61.35 ± 1.35	27.65 ± 2.39	45.36 ± 7.13
	2	53.96 ± 12.18	54.39 ± 11.37	58.97 ± 12.65	76.51 ± 1.31	42.63 ± 4.29	51.93 ± 4.21
	5	68.14 ± 6.95	64.79 ± 5.16	66.07 ± 6.16	**89.06 ± 0.69**	64.83 ± 1.62	78.26 ± 1.93
	10	75.04 ± 5.03	68.90 ± 5.08	70.74 ± 3.11	**89.68 ± 0.39**	74.66 ± 1.29	84.38 ± 1.75
	20	80.04 ± 2.54	72.02 ± 2.82	74.55 ± 3.09	**91.33 ± 0.36**	79.98 ± 0.96	91.29 ± 0.67
MoNet (Monti et al., 2017)	1	47.72 ± 15.53	39.13 ± 11.37	56.47 ± 4.67	58.99 ± 5.17	23.78 ± 7.57	34.72 ± 8.18
	2	60.85 ± 14.01	48.52 ± 9.52	61.03 ± 6.93	76.57 ± 4.06	38.19 ± 3.72	43.03 ± 8.22
	5	73.86 ± 7.97	61.66 ± 6.61	67.92 ± 2.50	87.02 ± 1.67	59.38 ± 4.73	71.80 ± 5.02
	10	78.82 ± 5.38	68.08 ± 6.29	71.24 ± 1.54	88.76 ± 0.49	68.66 ± 3.30	78.66 ± 3.17
	20	82.07 ± 2.03	71.52 ± 4.11	76.49 ± 1.75	90.31 ± 0.41	73.66 ± 2.87	88.61 ± 1.18

E.3 F-CDE

Drawing inspiration from the graph neural CDE model (Zhao et al., 2023), we further define the F-CDE model as follows:

$$D_t^{\beta}\mathbf{X}(t) = (\mathbf{A}(\mathbf{X}(t)) - \mathbf{I})\mathbf{X}(t) + \mathrm{div}(\mathbf{V}(t) \circ \mathbf{X}(t)) \tag{44}$$

In this expression, $\mathbf{V}(t)$ represents the velocity field of the graph at time t. The divergence operator, $\mathrm{div}(\cdot)$, is defined as per the formulation given in (Song et al., 2022), and $\circ$ symbolizes the element-wise (Hadamard) product.

We follow the same experimental setting as in the CDE paper(Zhao et al., 2023). Given that the primary focus of CDE is on evaluating model performance on **large heterophilic datasets**, our experiments are also conducted under similar conditions. The statistics for the dataset are available in Table 21. The sole distinction in our approach lies in incorporating fractional dynamics; we achieve this by replacing the ODE used in CDE with our FROND fractional derivative. The complete comparison results in Table 22 conspicuously reveal that Fractional CDE exhibits superior performance compared to the conventional CDE and other baselines across various datasets.

Table 21: Dataset statistics used in Table 4

Dataset	Nodes	Edges	Classes	Node Features
Roman-empire	22662	32927	18	300
Wiki-cooc	10000	2243042	5	100
Minesweeper	10000	39402	2	7
Questions	48921	153540	2	301
Workers	11758	519000	2	10
Amaon-ratings	24492	93050	5	300

Table 22: Full table: Node classification accuracy(%) of large heterophilic datasets.

Model	Roman-empire	Wiki-cooc	Minesweeper	Questions	Workers	Amazon-ratings
ResNet	65.71±0.44	89.36±0.71	50.95±1.12	70.10±0.75	73.08±1.28	45.70±0.69
H2GCN(Zhu et al., 2020a)	68.09±0.29	89.24±0.32	89.95±0.38	66.66±1.84	81.76±0.68	41.36±0.47
CPGNN(Zhu et al., 2021)	63.78±0.50	84.84±0.66	71.27±1.14	67.09±2.63	72.44±0.80	44.36±0.35
GPR-GNN(Chien et al., 2020)	73.37±0.68	91.90±0.78	81.79±0.98	73.41±1.24	70.59±1.15	43.90±0.48
GloGNN(Li et al., 2022)	63.85±0.49	88.49±0.45	62.53±1.34	67.15±1.92	73.90±0.95	37.28±0.66
FAGCN(Bo et al., 2021)	70.53±0.99	91.88±0.37	89.69±0.60	**77.04±1.56**	81.87±0.94	46.32±2.50
GBK-GNN(Du et al., 2022)	75.87±0.43	97.81±0.32	83.56±0.84	72.98±1.05	78.06±0.91	43.47±0.51
ACM-GCN(Luan et al., 2022)	68.35±1.95	87.48±1.06	90.47±0.57	OOM	78.25±0.78	38.51±3.38
GRAND(Chamberlain et al., 2021a)	71.60±0.58	92.03±0.46	76.67±0.98	70.67±1.28	75.33±0.84	45.05±0.65
GraphBel(Song et al., 2022)	69.47±0.37	90.30±0.50	76.51±1.03	70.79±0.99	73.02±0.92	43.63±0.42
Diag-NSD(Bodnar et al., 2022)	77.50±0.67	92.06±0.40	89.59±0.61	69.25±1.15	79.81±0.99	37.96±0.20
ACMP(Wang et al., 2022b)	71.27±0.59	92.68±0.37	76.15±1.12	71.18±1.03	75.03±0.92	44.76±0.52
CDE	91.64±0.28	97.99±0.38	95.50±5.23	75.17±0.99	80.70±1.04	47.63±0.43
F-CDE	**93.06±0.55**	**98.73±0.68**	**96.04±0.25**	75.17±0.99	**82.68±0.86**	**49.01±0.56**
β for F-CDE	0.9	0.6	0.6	1.0	0.4	0.1

E.4 F-GREAD

Our FROND framework is also extendable to the GREAD model (Choi et al., 2023), as defined in (45).

$$D_t^{\beta}\mathbf{X}(t) = -\alpha\mathbf{L}(\mathbf{X}(t)) + \alpha r(\mathbf{X}(t)) \tag{45}$$

where $r(\mathbf{X}(t))$ represents a reaction term, and α is a trainable parameter used to emphasize each term.

We adhere to the same experimental setting outlined in the GREAD paper (Choi et al., 2023), concentrating exclusively on heterophilic datasets. We choose the Blurring-Sharpening (BS) as the reaction term to formulate both GREAD-BS and F-GREAD-BS, as GREAD-BS exhibits strong performance according to Table 4 in the GREAD paper (Choi et al., 2023). The results presented in Table 23 (refer to Table 24 for comprehensive comparisons with other baselines) demonstrate that our FROND framework enhances the performance of GREAD across all examined datasets.

Table 23: Node classification accuracy(%) of heterophilic datasets

Model	Chameleon	Squirrel	Film	Texas	Wisconsin
GREAD-BS	71.38±1.31	59.22±1.44	37.90±1.17	88.92±3.72	89.41±3.30
F-GREAD-BS	**71.45±1.98**	**60.86±1.05**	**38.28±0.74**	**92.97±4.39**	**90.59±3.80**
β	0.9	0.9	0.8	0.9	0.9

Table 24: Full table: Node classification accuracy(%) of heterophilic datasets

Model	Chameleon	Squirrel	Film	Texas	Wisconsin
Geom-GCN(Pei et al., 2020)	60.00±2.81	38.15±0.92	31.59±1.15	66.76±2.72	64.51±3.66
H2GCN(Zhu et al., 2020a)	60.11±2.15	36.48±1.86	35.70±1.00	84.86±7.23	87.65±4.98
GGCN(Yan et al., 2022)	71.14±1.84	55.17±1.58	37.54±1.56	84.86±4.55	86.86±3.29
LINKX(Lim et al., 2021)	68.42±1.38	**61.81±1.80**	36.10±1.55	74.60±8.37	75.49±5.72
GloGNN(Li et al., 2022)	69.78±2.42	57.54±1.39	37.35±1.30	84.32±4.15	87.06±3.53
ACM-GCN(Luan et al., 2022)	66.93±1.85	54.40±1.88	36.28±1.09	87.84±4.40	88.43±3.22
GCNII(Chen et al., 2020)	63.86±3.04	38.47±1.58	37.44±1.30	77.57±3.83	80.39±3.40
CGNN(Xhonneux et al., 2020)	46.89±1.66	29.24±1.09	35.95±0.86	71.35±4.05	74.31±7.26
GRAND(Chamberlain et al., 2021a)	54.67±2.54	40.05±1.50	35.62±1.01	75.68±7.25	79.41±3.64
BLEND(Chamberlain et al., 2021b)	60.11±2.09	43.06±1.39	35.63±1.01	83.24±4.65	84.12±3.56
Sheaf(Bodnar et al., 2022)	68.04±1.58	56.34±1.32	37.81±1.15	85.05±5.51	89.41±4.74
GRAFF(Di Giovanni et al., 2022)	71.08±1.75	54.52±1.37	36.09±0.81	88.38±4.53	87.45±2.94
GREAD-BS	71.38±1.31	59.22±1.44	37.90±1.17	88.92±3.72	89.41±3.30
F-GREAD-BS	**71.45±1.98**	60.86±1.05	**38.28±0.74**	**92.97±4.39**	**90.59±3.80**
β	0.9	0.9	0.8	0.9	0.9

E.5 F-GRAPHCON

We also incorporate the following fractional-order oscillators dynamics, inspired by (Radwan et al., 2008; Rusch et al., 2022):

$$\begin{aligned} D_t^\beta \mathbf{Y} &= \sigma\left(\mathbf{F}_\theta(\mathbf{X}, t)\right) - \gamma \mathbf{X} - \alpha \mathbf{Y} \\ D_t^\beta \mathbf{X} &= \mathbf{Y} \end{aligned} \tag{46}$$

which represent the fractional dynamics version of GraphCON (Rusch et al., 2022). We denote this as F-GraphCON, with two variants, F-GraphCON-GCN and F-GraphCON-GAT. Here, $\mathbf{F}_\theta$ is set as GCN and GAT, as in the setting described in (Rusch et al., 2022). We refer readers to (Rusch et al., 2022) for further details. Notably, when $\beta = 1$, F-GraphCON simplifies to GraphCON, devoid of memory functionality.

Table 25: Node classification accuracy(%) based on GraphCON model

	Cora	Citeseer	Pubmed	Airport	Disease
GraphCON-GCN	81.9±1.7	72.9±2.1	78.8±2.6	68.6±2.1	87.5±4.1
GraphCON-GAT	83.2±1.4	73.2±1.8	79.4±1.3	74.1±2.7	65.7±5.9
F-GraphCON-GCN	**84.6±1.4**	**75.3±1.1**	**80.3±1.3**	**97.3±0.5**	**92.1±2.8**
β	0.9	0.8	0.9	0.1	0.1
F-GraphCON-GAT	83.9±1.2	73.4±1.5	79.4±1.3	97.3±0.8	86.9±4.0
β	0.7	0.9	1.0	0.1	0.1

Table 26: Full table: Node classification accuracy(%) based on GraphCON model.

	Cora	Citeseer	Pubmed	Airport	Disease
GCN	81.5±1.3	71.9±1.9	77.8±2.9	81.6±0.6	69.8±0.5
GAT	81.8±1.3	71.4±1.9	78.7±2.3	81.6±0.4	70.4±0.5
HGCN	78.7±1.0	65.8±2.0	76.4±0.8	85.4±0.7	89.9±1.1
GIL	82.1±1.1	71.1±1.2	77.8±0.6	91.5±1.7	90.8±0.5
GRAND-l	83.6±1.0	73.4±0.5	78.8±1.7	80.5±9.6	74.5±3.4
GRAND-nl	82.3±1.6	70.9±1.0	77.5±1.8	90.9±1.6	81.0±6.7
GraphCON-GCN	81.9±1.7	72.9±2.1	78.8±2.6	68.6±2.1	87.5±4.1
GraphCON-GAT	83.2±1.4	73.2±1.8	79.4±1.3	74.1±2.7	65.7±5.9
F-GraphCON-GCN	**84.6±1.4**	**75.3±1.1**	**80.3±1.3**	**97.3±0.5**	**92.1±2.8**
β	0.9	0.8	0.9	0.1	0.1
F-GraphCON-GAT	83.9±1.2	73.4±1.5	79.4±1.3	97.3±0.8	86.9±4.0
β	0.7	0.9	1.0	0.1	0.1

E.6 F-FLODE

Table 27: Node classification accuracy(%) of undirected graphs based on F-FLODE model

	Film	Squirrel	Chameleon
FLODE	37.16±1.42	64.23±1.84	73.60±1.55
F-FLODE	**37.95±1.27**	**65.53±1.83**	**74.17±1.59**
β	0.8	0.9	0.9

In the work of (Maskey et al., 2023), the authors introduce the FLODE model, which incorporates fractional graph shift operators within integer-order continuous GNNs. Specifically, instead of utilizing a Laplacian matrix $\mathbf{L}$, they employ the fractional power of $\mathbf{L}$, denoted as $\mathbf{L}^\alpha$ (see (47)). Our research diverges from this approach, focusing on the incorporation of time-fractional derivative D_t^β for updating graph node features in a memory-inclusive dynamical process. It is pivotal to differentiate the term "fractional" as used in our work from that in (Maskey et al., 2023), as they

Table 28: Node classification accuracy(%) of directed graphs based on F-FLODE model

	Film	Squirrel	Chameleon
FLODE	37.41±1.06	74.03±1.58	77.98±1.05
F-FLODE	**37.97±1.15**	**75.03±1.42**	**78.51±1.09**
β	0.9	0.9	0.9

signify fundamentally distinct concepts in the literature. Fundamentally, FLODE differs from our work in key aspects:

- FLODE employs the fractional (real-valued) power of $\mathbf{L}$, namely $\mathbf{L}^\alpha$. The feature evolution model used by FLODE, specifically in its first heat diffusion-type variant, is given by:
$$\frac{\mathrm{d}\mathbf{X}(t)}{\mathrm{d}t} = -\mathbf{L}^\alpha \mathbf{X}(t)\mathbf{\Phi}. \tag{FLODE}$$
This is a graph spatial domain rewiring technique, as $\mathbf{L}^\alpha$ introduces dense connections compared to $\mathbf{L}$. As a result, FLODE introduces space-based long-range interactions during the feature updating process.
- In contrast, our FROND model incorporates the time-fractional derivative D_t^β to update graph node features in a memory-inclusive dynamical process. In this context, time acts as a continuous counterpart to the layer index, leading to significant dense skip connections between layers due to memory dependence. Thus, FROND induces time/layer-based long-range interactions in the feature update process. Note that FLODE does not utilize time-fractional derivatives. Our method is not only *compatible with various integer-order continuous GNNs, including FLODE (see* (F-FLODE)*),* but also extends them to graph FDE models.

We next introduce the F-FLODE model, which utilizes time-fractional derivatives for updating graph node features in FLODE:
$$D_t^\beta \mathbf{X}(t) = -\mathbf{L}^\alpha \mathbf{X}(t)\mathbf{\Phi}, \tag{F-FLODE}$$
where $\mathbf{L}$ denotes the symmetrically normalized adjacency matrix. The α-fractional power of the graph Laplacian, $\mathbf{L}^\alpha$, is given by:
$$\mathbf{L}^\alpha := \mathbf{U}\mathbf{\Sigma}^\alpha \mathbf{V}^{\mathrm{H}}. \tag{47}$$
In this formulation, $\mathbf{U}$, $\mathbf{\Sigma}$, and $\mathbf{V}$ are obtained from the SVD decomposition of $\mathbf{L} = \mathbf{U}\mathbf{\Sigma}\mathbf{V}^{\mathrm{H}}$, and $\alpha \in \mathbb{R}$ represents the order. The channel mixing matrix $\mathbf{\Phi}$, a symmetric matrix, follows the setting in (Maskey et al., 2023).

Following the experimental setup outlined in (Maskey et al., 2023), we present our results in Tables 27 and 28, demonstrating that our FROND framework enhances the performance of FLODE across all evaluated datasets. Note the difference in the equations in (FLODE) and (F-FLODE), where the two are equivalent only when $\beta = 1$. This example illustrates that the FROND framework encompasses the FLODE model as a special case when $\beta = 1$. Our experimental results indicate that F-FLODE outperforms FLODE with the optimal $\beta \neq 1$ in general.

F Proofs of Results

In this section, we provide detailed proofs of the results stated in the main paper.

F.1 Proof of Theorem 1

Proof. We observe that for $0 < \beta < 1$ they possess the properties, the coefficients c_k, b_m defined in (10) satisfying the following properties.
$$\sum_{k=1}^{\infty} c_k = 1, \quad 1 > \beta = c_1 > c_2 > c_3 > \ldots \to 0,$$
$$b_0 = 1, \quad b_m = 1 - \sum_{k=1}^{m} c_k = \sum_{k=m+1}^{\infty} c_k, 1 = b_0 > b_1 > b_2 > b_3 > \ldots \to 0.$$

From the definition of the transition probability (11), we have

$$\begin{aligned}
&\mathbb{P}(\mathbf{R}(t_{n+1}) = \mathbf{x}_h(0)) \\
&= b_n \mathbb{P}(\mathbf{R}(t_0) = \mathbf{x}_h(0)) + c_n \mathbb{P}(\mathbf{R}(t_1) = \mathbf{x}_h(0)) + \ldots + c_2 \mathbb{P}(\mathbf{R}(t_{n-1}) = \mathbf{x}_h(0)) + \\
&\quad + (c_1 - \sigma^\beta)\mathbb{P}(\mathbf{R}(t_n) = \mathbf{x}_h(0)) + \sum_{j=1}^{n} \sigma^\beta \frac{W_{jh}}{d_j} \mathbb{P}(\mathbf{R}(t_n) = \mathbf{x}_j(0)) \\
&= b_n \mathbb{P}(\mathbf{R}(t_0) = \mathbf{x}_h(0)) + c_n \mathbb{P}(\mathbf{R}(t_1) = \mathbf{x}_h(0)) + \ldots + c_2 \mathbb{P}(\mathbf{R}(t_{n-1}) = \mathbf{x}_h(0)) + \\
&\quad + c_1 \mathbb{P}(\mathbf{R}(t_n) = \mathbf{x}_h(0)) - \sigma^\beta \mathbb{P}(\mathbf{R}(t_n) = \mathbf{x}_h(0)) + \sum_{j=1}^{N} \sigma^\beta \frac{W_{jh}}{d_j} \mathbb{P}(\mathbf{R}(t_n) = \mathbf{x}_j(0)). \qquad (48)
\end{aligned}$$

By rearranging, we have

$$\begin{aligned}
&\mathbb{P}(\mathbf{R}(t_{n+1}) = \mathbf{x}_h(0)) - \sum_{k=1}^{n} c_k \mathbb{P}(\mathbf{R}(t_{n+1-k}) = \mathbf{x}_h(0)) - b_n \mathbb{P}(\mathbf{R}(t_0) = \mathbf{x}_h(0)) \\
&= (-1)^0 \binom{\beta}{0} \mathbb{P}(\mathbf{R}(t_{n+1}) = \mathbf{x}_h(0)) - \sum_{k=1}^{n} (-1)^{k+1} \binom{\beta}{k} \mathbb{P}(\mathbf{R}(t_{n+1-k}) = \mathbf{x}_h(0)) \\
&\qquad - \sum_{k=0}^{n} (-1)^k \binom{\beta}{k} \mathbb{P}(\mathbf{R}(0) = \mathbf{x}_h(0)) \\
&= \sum_{k=0}^{n} (-1)^k \binom{\beta}{k} \mathbb{P}(\mathbf{R}(t_{n+1-k}) = \mathbf{x}_h(0)) - \sum_{k=0}^{n} (-1)^k \binom{\beta}{k} \mathbb{P}(\mathbf{R}(0) = \mathbf{x}_h(0)) \\
&= \sum_{k=0}^{n} (-1)^k \binom{\beta}{k} \left[\mathbb{P}(\mathbf{R}(t_{n+1-k}) = \mathbf{x}_h(0)) - \mathbb{P}(\mathbf{R}(0) = \mathbf{x}_h(0))\right] \\
&= -\sigma^\beta \mathbb{P}(\mathbf{R}(t_n) = \mathbf{x}_h(0)) + \sum_{j=1}^{n} \sigma^\beta \frac{W_{jh}}{d_j} \mathbb{P}(\mathbf{R}(t_n) = \mathbf{x}_j(0)).
\end{aligned}$$

Dividing both sides of the final equality by σ^β, it follows that

$$\begin{aligned}
&\sum_{k=0}^{n} (-1)^k \binom{\beta}{k} \frac{\mathbb{P}(\mathbf{R}(t_{n+1-k}) = \mathbf{x}_h(0)) - \mathbb{P}(\mathbf{R}(0) = \mathbf{x}_h(0))}{\sigma^\beta} \\
&= -\mathbb{P}(\mathbf{R}(t_n) = \mathbf{x}_h(0)) + \sum_{j=1}^{N} \frac{W_{jh}}{d_j} \mathbb{P}(\mathbf{R}(t_n) = \mathbf{x}_j(0)). \qquad (49)
\end{aligned}$$

From the Griinwald-Letnikov fractional derivatives formulation (Podlubny, 1999)[eq. (2.54)], the limit of LHS of (49) is

$$\lim_{\substack{\sigma \to 0 \\ n\sigma = t}} \sum_{k=0}^{n} (-1)^k \binom{\beta}{k} \frac{\mathbb{P}(\mathbf{R}(t_{n+1-k}) = \mathbf{x}_h(0)) - \mathbb{P}(\mathbf{R}(0) = \mathbf{x}_h(0))}{\sigma^\beta} = D_t^\beta \mathbb{P}(\mathbf{R}(t) = \mathbf{x}_h(0)). \qquad (50)$$

On the other hand, the RHS of (49) is

$$-\mathbb{P}(\mathbf{R}(t_n) = \mathbf{x}_h(0)) + \sum_{j=1}^{N} \frac{W_{jh}}{d_j} \mathbb{P}(\mathbf{R}(t_n) = \mathbf{x}_j(0)) = [-\mathbf{L}\mathbb{P}(\mathbf{R}(t_n))]_h \qquad (51)$$

where $\mathbb{P}(\mathbf{R}(t_n))$ is the probability (column) vector with j-th element being $\mathbb{P}(\mathbf{R}(t_n) = \mathbf{x}_j(0))$, and $[-\mathbf{L}\mathbb{P}(\mathbf{R}(t_n))]_h$ denotes the h-th element of the vector $-\mathbf{L}\mathbb{P}(\mathbf{R}(t_n))$.

Putting them together, we have

$$D_t^\beta \mathbb{P}(\mathbf{R}(t)) = -\mathbf{L}\mathbb{P}(\mathbf{R}(t)) \qquad (52)$$

since we assume $t_n = t$ in the limit. Finally, from the linearity of the operator D_t^β and $\mathbf{L}$, we have

$$D_t^\beta \mathbb{P}(\mathbf{R}(t))\mathbf{X}(0) = -\mathbf{L}\mathbb{P}(\mathbf{R}(t))\mathbf{X}(0), \qquad (53)$$

which states that $D_t^\beta \mathbb{E}\mathbf{R}(t) = -\mathbf{L}\mathbb{E}\mathbf{R}(t)$ for any probability distribution $\mathbb{P}(\mathbf{R}(0))$. For each i, if $\mathbf{R}(t_0) = \mathbf{x}_i$ with probability one, the initial condition of (9) is satisfied. The proof of Theorem 1 is now complete. □

F.2 PROOF OF THEOREM 2

Before presenting the formal proof, we aim to provide additional insights and intuition regarding the algebraic convergence from two perspectives.

- Fractional Random Walk Perspective: In a standard random walk, a walker moves to a new position at each time step without delay. However, in a fractional random walk, which is more reflective of our model's behavior, the walker has a probability of revisiting past positions. This revisitation is not arbitrary; it's governed by a waiting time that follows a power-law distribution with a long tail. This characteristic fundamentally changes the walk's dynamics, introducing a memory component and leading to a slower, algebraic rate of convergence. This behavior is intrinsically different from normal random walks, where the absence of waiting times facilitates a quicker, often exponential, convergence.

- Analytic Perspective: From an analytic perspective, the essential slow algebraic rate primarily stems from the slow convergence of the Mittag-Leffler function towards zero. To elucidate this, let us consider the scalar scenario. Recall that the Mittag-Leffler function E_β is defined as:
$$E_\beta(z) := \sum_{j=0}^{\infty} \frac{z^j}{\Gamma(j\beta+1)}$$
for values of z where the series converges. Specifically, when $\beta = 1$,
$$E_1(z) = \sum_{j=0}^{\infty} \frac{z^j}{\Gamma(j+1)} = \sum_{j=0}^{\infty} \frac{z^j}{j!} = \exp(z)$$
corresponds to the well-known exponential function. According to [A1, Theorem 4.3.], the eigenfunctions of the Caputo derivative are expressed through the Mittag-Leffler function. In more precise terms, if we define $y(t)$ as
$$y(t) := E_\beta\left(-\lambda t^n\right), \quad t \geq 0,$$
it follows that
$$D_t^\beta y(t) = -\lambda y(t).$$
Notably, when $\beta = 1$, this reduces to $\frac{\mathrm{d}\exp(-\lambda t)}{\mathrm{d}t} = -\lambda \exp(-\lambda t)$. We examine the behavior of $E_\beta\left(-\lambda t^n\right)$. From (Diethelm, 2010)[Theorem 7.3.], it is noted that:

  (a) The function $y(t)$ is completely monotonic on $(0, \infty)$.

  (b) As $x \to \infty$,
$$y(t) = \frac{t^{-\beta}}{\lambda\Gamma(1-\beta)}(1 + o(1)).$$
Thus, the function $E_\beta\left(-\lambda t^\beta\right)$ converges to zero at a rate of $\Theta\left(t^{-\beta}\right)$. Our paper extends this to the general high-dimensional case by replacing the scalar λ with the Laplacian matrix $\mathbf{L}$, wherein the eigenvalues of $\mathbf{L}$ play a critical role analogous to λ in the scalar case.

  For a diagonalizable Laplacian matrix $\mathbf{L}$, the proof essentially reverts to the scalar case as outlined above (refer to (56) in our paper). However, in scenarios where $\mathbf{L}$ is non-diagonalizable and has a general Jordan normal form, it becomes necessary to employ the Laplace transform technique to demonstrate that the algebraic rate remains valid (refer to the context between (56) and (57) in our paper).

Proof. We first prove the stationary probability $\boldsymbol{\pi} = \left(\frac{d_1}{\sum_{j=1}^N d_j}, \ldots, \frac{d_N}{\sum_{j=1}^N d_j}\right)$ by induction. Assume that for $i = 1, \ldots, n$, the probability distribution $\mathbb{P}(\mathbf{R}(t_n))$ always equals $\boldsymbol{\pi}^\intercal$. For $i = n+1$, from (48), it follows that
$$\begin{aligned}
[\mathbb{P}(\mathbf{R}(t_{n+1}))]_h &= \mathbb{P}(\mathbf{R}(t_{n+1}) = \mathbf{x}_h(0)) \\
&= b_n \mathbb{P}(\mathbf{R}(t_0) = \mathbf{x}_i(0)) + \sum_k c_k \mathbb{P}(\mathbf{R}(t_{n+1-k}) = \mathbf{x}_h(0)) \\
&\quad - \sigma^\beta \mathbb{P}(\mathbf{R}(t_n) = \mathbf{x}_h(0)) + \sum_{j=1}^N \sigma^\beta \frac{W_{jh}}{d_j} \mathbb{P}(\mathbf{R}(t_n) = \mathbf{x}_j(0))
\end{aligned}$$

$$
\begin{aligned}
&= \boldsymbol{\pi}_h b_n + \sum_{k=1}^{n} \boldsymbol{\pi}_h c_k - \boldsymbol{\pi}_h \sigma^\beta + \sum_{j=1, j\neq h}^{N} \boldsymbol{\pi}_j \sigma^\beta \frac{W_{jh}}{d_j} \\
&= \boldsymbol{\pi}_h (b_n + \sum_{k=1}^{n} c_k) - \boldsymbol{\pi}_h \sigma^\beta + \sum_{j=1, j\neq h}^{N} \frac{d_j}{\sum_{j=1}^{N} d_j} \sigma^\beta \frac{W_{jh}}{d_j} \\
&= \boldsymbol{\pi}_h - \boldsymbol{\pi}_h \sigma^\beta + \sigma^\beta \sum_{j=1, j\neq h}^{N} \frac{W_{jh}}{\sum_{j=1}^{N} d_j} \\
&= \boldsymbol{\pi}_h - \boldsymbol{\pi}_h \sigma^\beta + \sigma^\beta \frac{d_h}{\sum_{j=1}^{N} d_j} \\
&= \boldsymbol{\pi}_h.
\end{aligned}
$$

This proves the existence of stationary probability. The uniqueness follows from this observation: if $\mathbb{P}(\mathbf{R}(t_1)) = \boldsymbol{\pi}' \neq \boldsymbol{\pi}$, we do not have $\mathbb{P}(\mathbf{R}(t_2)) = \mathbb{P}(\mathbf{R}(t_1))$ since otherwise it indicates that the Markov chain defined by

$$
\begin{aligned}
&\mathbb{P}\big(\mathbf{R}(t_{n+1}) = \mathbf{x}_{(j_{n+1})}(0) \,\big|\, \mathbf{R}(t_n) = \mathbf{x}_{(j_n)}(0)\big) = \mathbb{P}\big(\mathbf{R}(t_{n+1}) = \mathbf{x}_{(j_2)}(0) \,\big|\, \mathbf{R}(t_n) = \mathbf{x}_{(j_1)}(0)\big) \\
&= \begin{cases} c_1 - \sigma^\beta + b_1 & \text{if staying at current location with } j_{n+1} = j_n \\ \sigma^\beta \frac{W_{j_n j_{n+1}}}{d_{j_n}} & \text{if jumping to neighboring nodes with } j_{n+1} \neq j_n \end{cases}
\end{aligned} \tag{54}
$$

has stationary distribution other than $\boldsymbol{\pi}$, which contradicts the assumption of a strongly connected and aperiodic graph.

We now establish the algebraic convergence. Consider $\mathbf{L} = \mathbf{S}\mathbf{J}\mathbf{S}^{-1}$ as the Jordan canonical form of $\mathbf{L}$. It is evident that for the matrix $\mathbf{W}\mathbf{D}^{-1}$, since $\mathbf{W}\mathbf{D}^{-1}$ is left stochastic and the graph is strongly connected and aperiodic, the Perron-Frobenius theorem (Horn & Johnson, 2012)[Lemma 8.4.3., Theorem 8.4.4] confirms that the value 1 is the sole eigenvalue of it that equals the spectral radius 1. Hence, we have that $\mathbf{L} = \mathbf{I} - \mathbf{W}\mathbf{D}^{-1}$ possesses an eigenvalue of 0, and all the remaining eigenvalues have positive real parts. Consequently, $\mathbf{J}$ contains a block that consists of only a single 0. We can rewrite (52) as

$$
D_t^\beta \mathbf{Y}(t) = -\mathbf{J}\mathbf{Y}(t) \tag{55}
$$

where $\mathbf{S}^{-1}\mathbb{P}(\mathbf{R}(t)) = \mathbf{Y}(t) \in \mathbb{R}^N$ and the inital condition is $\mathbf{S}^{-1}\mathbb{P}(\mathbf{R}(0)) = \mathbf{Y}(0)$.

If $\mathbf{L}$ is diagonalizable, then $\mathbf{J}$ is a diagonal matrix with the diagonal elements being the eigenvalues. We have an uncoupled set of equations in the form $D_t^\beta \mathbf{Y}_k(t) = -\lambda_k \mathbf{Y}_k(t)$, where $\mathbf{Y}_k$ is the k-th component of $\mathbf{Y}$. According to (Podlubny, 1999), the solution is given by

$$
\mathbf{Y}_k(t) = \mathbf{Y}_k(0) E_\beta(-\lambda_k t^\beta) \tag{56}
$$

where $E_\beta(\cdot)$ is the Mittag-Leffler function define as $E_\beta(z) = \sum_{j=0}^{\infty} \frac{z^j}{\Gamma(\beta j+1)}$ and $\Gamma(\cdot)$ is the gamma function. For the index w s.t. the eigenvalue $\lambda_w = 0$, we have the solution $\mathbf{Y}_k(t) = \mathbf{Y}_k(0)$ which corresponds to the stationary probability vector if we transform it back to $\mathbb{P}(\mathbf{R}(t))$. From (Mainardi, 2014), we have that for $k \neq w$, the convergence to 0 is in the following order

$$
\mathbf{Y}_k(t) = \Theta(t^{-\beta}).
$$

If $\mathbf{J}$ is not diagonal, the entries of $\mathbf{Y}(t)$ that correspond to distinct Jordan blocks in $\mathbf{J}$ are not coupled. W.L.O.G, we assume the first Jordan block is associated to eigenvalue $\lambda_1 = 0$, while all eigenvalues $\lambda_k > 0$, for $k = 2, \ldots, N$. A consideration of the Jordan block corresponding to one λ_k, $k = 2, \ldots, N$, is adequate. We assume the Jordan block $\mathbf{J}(\lambda_k)$ corresponding to λ_k has size m. It follows that for this Jordan block we have

$$
\begin{aligned}
D_t^\beta \mathbf{Y}_1(t) &= \lambda_k \mathbf{Y}_1(t) + \mathbf{Y}_2(t), \\
&\vdots \\
D_t^\beta \mathbf{Y}_{m-1}(t) &= \lambda_k \mathbf{Y}_{m-1}(t) + \mathbf{Y}_m(t), \\
D_t^\beta \mathbf{Y}_m(t) &= \lambda_k \mathbf{Y}_m(t),
\end{aligned}
$$

which can be solved from the bottom up. Starting with the last equation, we have

$$
\mathbf{Y}_m(t) = \mathbf{Y}_m(0) E_\beta(-\lambda_k t^\beta) = \Theta(t^{-\beta}).
$$

Furthermore, we have

$$
D_t^\beta \mathbf{Y}_{m-1}(t) = \lambda_k \mathbf{Y}_{m-1}(t) + \mathbf{Y}_m(0) E_\beta(-\lambda_k t^\beta).
$$

Applying the Laplace transform yields

$$\mathcal{L}\left\{D_t^{\beta}\mathbf{Y}_{m-1}(t)\right\} = s^{\beta}Y_{m-1}(s) - s^{\beta-1}\mathbf{Y}_{m-1}(0)$$

where $Y_{m-1}(s)$ is the Laplace transform of $\mathbf{Y}_{m-1}(t)$ according to (3). Now, for the right hand side, we have $L\{\lambda\mathbf{Y}_{m-1}(t)\} = \lambda_k Y_{m-1}(s)$ and we know that the Laplace transform of $E_{\beta}\left(-\lambda_k t^{\beta}\right)$ is $\frac{s^{\beta-1}}{(s^{\beta}+\lambda_k)}$. Therefore, the equation in the Laplace domain becomes:

$$s^{\beta}Y_{m-1}(s) - s^{\beta-1}\mathbf{Y}_{m-1}(0) = \lambda_k Y_{m-1}(s) + \mathbf{Y}_m(0)\frac{s^{\beta-1}}{s^{\beta}+\lambda_k}.$$

Rearranging this equation to solve for $Y_{m-1}(s)$ gives:

$$Y_{m-1}(s) = \frac{s^{\beta-1}\mathbf{Y}_{m-1}(0) + \mathbf{Y}_m(0)\frac{s^{\beta-1}}{s^{\beta}+\lambda_k}}{s^{\beta}+\lambda_k}.$$

It follows that $Y_{m-1}(s) \sim Cs^{\beta-1}$ when $s \to 0$. We can repeat the above process to show that $Y_i(s) \sim Cs^{\beta-1}$ when $s \to 0$ for all $i = 1, \ldots, m-2$. According to the Hardy–Littlewood Tauberian theorem (Wikipedia, 2023), we have that, for all $i = 1, \ldots, m$,

$$\mathbf{Y}_i(t) = \Theta(t^{-\beta}). \tag{57}$$

The proof is now complete. □

F.3 Proof of Corollary 1

We are unable to directly invoke (15) to infer $\mathbf{E}(\mathbf{X}(t)) = \Theta(t^{-2\beta})$ in (17) since it only yields an upper bound, as presented below:

$$\|\mathbf{x}_i(t) - \mathbf{x}_j(t)\|_2^2 \leq \left(\|\mathbf{x}_i(t) - \mathbf{x}_{\mathbf{s}}\|_2 + \|\mathbf{x}_j(t) - \mathbf{x}_{\mathbf{s}}\|_2\right)^2. \tag{58}$$

Consequently, we directly refer to (55). We use the notation $\mathbf{e}_i$ to denote the one-hot vector where the i-th component stands at 1. Recall that we have the solution $\mathbb{P}_i(\mathbf{R}(t))$ with initial condition $\mathbf{e}_i$ for each i. The set $\{\mathbf{e}_i\}_{i=1}^N$ is linearly independent and spans the full $\mathbb{R}^N$ space. It is equivalent to getting the transformed solution $\mathbf{Y}_i(t)$ with the initial condition $\mathbf{S}^{-1}\mathbf{e}_i$ in (55). The entries of $\mathbf{Y}(t)$ that correspond to distinct Jordan blocks in $\mathbf{J}$ are not coupled. We denote the solution to (55) with initial condition $\mathbf{e}_k$ as $\bar{\mathbf{Y}}_{(k)}(t)$. Note, according to the proof of theorem 2, we have that the solution corresponds to the unique eigenvalue 0 to matrix $\mathbf{J}$ keep a constant. If we assume eigenvalue 0 is the first Jodan block, we have $\bar{\mathbf{Y}}_{(1)}(t) = \bar{\mathbf{Y}}_{(1)}(0)$ for all time $t \geq 0$. While all the other solutions $\bar{\mathbf{Y}}_{(k)}(t)$, $k = 2, ..., N$, corresponding to the other Jordan blocks, converge to 0 in $\Theta\left(t^{-\beta}\right)$ rate. From the linearity, we then have $\mathbf{Y}_i(t)$ are the linear combination of the N independent solutions $\{\bar{\mathbf{Y}}_{(k)}(t)\}_{i=1}^N$. More specifically, we have that

$$\mathbf{Y}_i(t) = [\mathbf{S}^{-1}\mathbf{e}_i]_0\bar{\mathbf{Y}}_1(0) + \sum_{k=2}^{N}[\mathbf{S}^{-1}\mathbf{e}_i]_k\Theta\left(t^{-\beta}\right)$$

where $[\mathbf{S}^{-1}\mathbf{e}_i]_k$ is the k-component of matrix $\mathbf{S}^{-1}\mathbf{e}_i$. We can prove that the first row of $\mathbf{S}^{-1}$ is $a\mathbf{1}^{\top}$ with a being a scalar and $\mathbf{1}$ is an all-ones vector (it is based on Horn & Johnson (2012)[Theorem 3.2.5.2.], see Lemma 1). It follows that $[\mathbf{S}^{-1}\mathbf{e}_i]_0$ is the same for all i. We therefore have that for some i and j,

$$\|\mathbf{x}_i(t) - \mathbf{x}_j(t)\|_2^2 = \|\mathbf{S}\mathbf{Y}_i(t) - \mathbf{S}\mathbf{Y}_j(t)\|^2 = \Theta\left(t^{-2\beta}\right).$$

The proof is now complete.

Lemma 1. *The first row of $\mathbf{S}^{-1}$ is $a\mathbf{1}^{\top}$ with a being a scalar and $\mathbf{1}$ is an all-ones vector.*

Proof. The Jordan canonical form of $\mathbf{W}\mathbf{D}^{-1}$ is represented as $\mathbf{S}\bar{\mathbf{J}}\mathbf{S}^{-1}$ where $\bar{\mathbf{J}} = \mathbf{J} + \mathbf{I}$ with the first Jordan block being 1 and the rest having eigenvalues *strictly less than* 1. Based on (Horn & Johnson, 2012)[Theorem 3.2.5.2.], we observe that $\lim_{k\to\infty}(\mathbf{W}\mathbf{D}^{-1})^k = \lim_{k\to\infty}\mathbf{S}\bar{\mathbf{J}}^k\mathbf{S}^{-1} = \mathbf{S}\mathbf{\Lambda}\mathbf{S}^{-1}$, where $\mathbf{\Lambda}$ is a diagonal matrix with the first element as 1 and all the others as 0:

$$\mathbf{\Lambda} = \begin{pmatrix} 1 & & & \\ & 0 & & \\ & & \ddots & \\ & & & 0 \end{pmatrix}.$$

Since $\lim_{k\to\infty}(\mathbf{W}\mathbf{D}^{-1})^k$ maintains its column stochasticity and the rank of $\mathbf{S}\mathbf{\Lambda}\mathbf{S}^{-1}$ is 1, we deduce that the first row of $\mathbf{S}^{-1}$ is $a\mathbf{1}^{\intercal}$ with a being a scalar and $\mathbf{1}$ an all-ones vector. □

LIMITATIONS

Our research proposes an advanced graph diffusion framework that integrates *time-fractional derivatives*, effectively encompassing many GNNs. Nonetheless, it presents certain limitations. A crucial element we have overlooked is the application of the *fractional derivative in the spatial domain*. In fractional diffusion equations, this implies substituting the standard second-order spatial derivative with a Riesz-Feller derivative (Gorenflo & Mainardi, 2003), thus modeling a random walk with space-based long-range jumps. Incorporating such a space-fractional diffusion equation within GNNs could potentially alleviate issues like the bottleneck and over-squashing highlighted in (Alon & Yahav, 2021). This represents a current limitation of our work and suggests a compelling future research trajectory that merges both time and space fractional derivatives in GNNs.

BROADER IMPACT

The introduction of FROND holds significant potential for applications such as sensor networks, transportation, and manufacturing. FROND's ability to encapsulate long-term memory in neural dynamical processes can enhance the representation of complex interconnections, improving predictive modeling and efficiency. This could lead to more responsive sensor networks, optimized routing in transportation, and improved visibility into manufacturing process networks. However, the advent of FROND and similar models may also have mixed labor implications. While these technologies might render certain repetitive tasks obsolete, potentially displacing jobs, they may also generate new opportunities focused on developing and maintaining such advanced systems. Moreover, the shift from mundane tasks could enable workers to focus more on strategic and creative roles, enhancing job satisfaction and productivity. It's paramount that the deployment of FROND is done ethically, with ample support for reskilling those whose roles may be affected. This helps ensure that the broader impact of this technology is beneficial to society as a whole.